Electron spins interaction in the spin-Peierls phase of the organic spin chain (o-DMTTF)2X (X = Cl, Br, I)

Loic Soriano, Olivier Pilone, Michael D. D Kuz'Min, Herve Vezin, Olivier Jeannin, Marc Fourmigué, Maylis Orio, Sylvain Bertaina

Electron spins interaction in the spin-Peierls phase of the organic spin chain (o-DMTTF)$_2X$ (X = Cl, Br, I)

L. Soriano,[1] O. Pilone,[1] M.D. Kuz'min,[1] H. Vezin,[2] O. Jeannin,[3] M. Fourmigué,[3] M. Orio,[4] and S. Bertaina[1,*]

[1] *CNRS, Aix-Marseille Université, IM2NP (UMR 7334), Institut Matériaux Microélectronique et Nanosciences de Provence, Marseille, France.*
[2] *CNRS, Université de Lille, LASIRE (UMR 8516), Laboratoire de Spectrochimie Infrarouge Raman et Environnement, Villeneuve d'Ascq, France*
[3] *Université de Rennes, CNRS, ISCR UMR 6226, F-35042 Rennes, France.*
[4] *CNRS, Aix-Marseille Université, Centrale Marseille, ISM2, Institut des science moléculaire de marseille, Marseille, France.*

(Dated: February 17, 2022)

We investigate the electron spin resonance of the organic spin-Peierls chain (o-DMTTF)$_2X$ with X = Cl, Br and I. We describe the temperature dependence of the spin gap during the phase transition and quantify the dimerization parameter δ. At the lowest temperatures, the susceptibility is governed by defects in the spin dimerized chain. Such strongly correlated defects are the consequence of breaks in the translational symmetry of the chain. In the vicinity of the defects the spins are polarized antiferomagnetically forming a magnetic soliton: a spin $\frac{1}{2}$ quasi-particle of size ruled by δ pinned to the defects. For (o-DMTTF)$_2$Br and (o-DMTTF)$_2$Cl, we show that the one-half of the total number of solitons are in isolation (as singles) whereas the other half form pairs (soliton dimers)with a strong magnetic coupling. The Rabi oscillations of both the single-soliton and the soliton-dimer are observed, which is a prerequisite in the context of quantum information.

I. INTRODUCTION

The physics of spin $S = \frac{1}{2}$ chains remains extremely rich because their low dimension leads to pronounced influence of the electronic correlation and allows the interplay between magnetic, electronic and lattice degree of freedom [1, 2]. In particular, in $S = \frac{1}{2}$ antiferromagnetic Heisenberg spin chains, the quantum fluctuation prevents long-range order and the ground state is gapless [3]. However, this sate is unstable and a weak coupling with the other chains or with the lattice opens a gap in the magnetic spectrum and leads to a long-range order (antiferromagnetic order) or to dimerization (spin-Peierls). The effect of defects in 1D spin systems continue to be actively studied because the break in the translation symmetry deeply alters the magnetic properties of the host materials [4]. In the spin-Peierls infinite chains, the ground state is a singlet ($S = 0$) separated from the quasi continuum by a gap [5, 6]. The break in the translational symmetry, like a chain-end or a stacking fault, alters the spins in the vicinity creating a magnetic soliton (spin-$\frac{1}{2}$ quasiparticle made of many correlated spins) pinned to the defects [7, 8]. As a consequence of this many-body spin-$\frac{1}{2}$ soliton formation, the ground state is a doublet separated from the quasicontinnum by a gap [9]. Such a structure is of particular interest because its energy levels are comparable to single molecular magnet SMM like V15 [10–12] with unconventional quantum coherence properties [13, 14] which make it an interesting potential qubit [15, 16].

Organic one-dimensional conductors were extensively studied over the past decades due to the richness of the phase diagram. One of the most famous is the Fabre salt (TMTTF)$_2X$, where X is a counter anion. Depending on the temperature, the pressure and the nature of X, (TMTTF)$_2X$ can be a metallic/insulator/superconductor uniform/dimerized spin chain, Néel-/charge-/anion-ordered ([17–22]). The defects in the spin chains have been observed by electron spin resonance (ESR) [23, 24] but due to a low spin-Peierls transition temperature T_{SP} and to a high homogeneity of the ESR line, the quantum coherence study is limited.

The (o-DMTTF)$_2X$ family compounds, with X = Cl, Br and I, have $T_{SP} \sim 50$ K higher than (TMTTF)$_2$PF$_6$ (T_{SP} = 19 K) which itself has the highest T_{SP} of the (TMTTF)$_2X$ series. Moreover electron spin echo of the pined soliton has been reported [14]. (o-DMTTF)$_2X$ was first synthesized many decades ago [25] but intensive studies have been published recently [26] with the construction of the phase diagram [27, 28], the solid solution with different counter anion [29] and the ESR study[12, 14]

The three systems (o-DMTTF)$_2X$ crystallize in the same space group $I\bar{4}2d$ (no. 122) with cell parameters $a = b$ = 16.93 Å, 17.09 Å, 17.40 Å and c = 7.040 Å, 7.058 Å, 7.098 Å for (o-DMTTF)$_2$Cl, (o-DMTTF)$_2$Br and (o-DMTTF)$_2$I respectively. The halide anions X are in position $\bar{4}$ while $o-$DMTTF molecules lie on the two-fold axis forming a stack in the direction c. Each linear stack is turned by 90° with respect to its neighbors, as shown in Fig. 1. This "chessboard" structure has a consequence of a very weak inter-stack interactions compared to the parallel stack of the famous (TMTTF)$_2X$, confirmed by the highly anisotropic conductivity of (o-DMTTF)$_2X$ [27, 28]. Each pair of $o-$(DMTTF)$_2$ shares a spin $S = \frac{1}{2}$ and forms a quasi-isotropic Heisenberg spin chain along c-axis. When $T < T_{SP}$ the displacement of the pairs of $o-$(DMTTF)$_2$ creates the tetramerization

* sylvain.bertaina@cnrs.fr

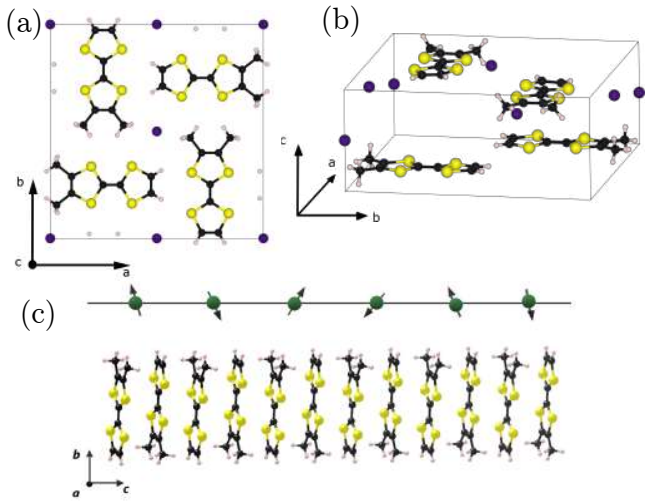

Figure 1. Crystallographic structure of $(o\text{-DMTTF})_2X$. (a) View of the ab plane and (b) perspective view of the unit cell with four DMTTF in equivalent positions rotated by 90°. The DMTTF molecules are stacked along c axis but only 4 molecules are shown to avoid confusions. (c) Stacks of $(DMTTF)_2$ along the c axis. Each pair of $(DMTTF)_2$ shares a spin $S = \frac{1}{2}$ forming a spin chain along c.

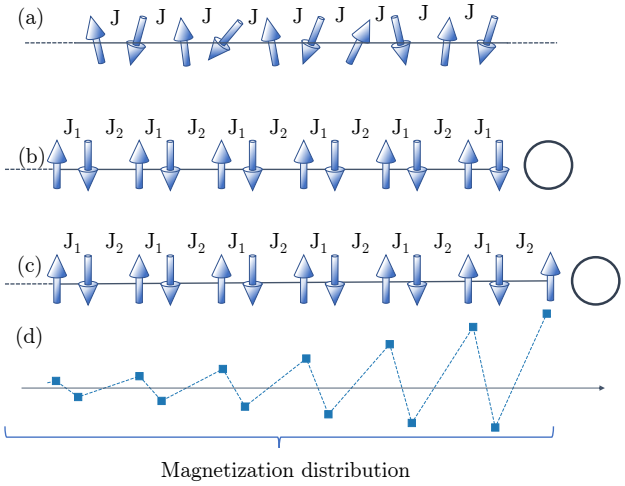

Figure 2. Schematic representation of the spin chain during the spin-Peierls transition and the defect-induced soliton formation. (a) For $T > T_{SP}$, the uniform Heisenberg spin chain is made of constant exchange coupling J between equidistant nearest-neighbor spins. (b)and (c) For $T < T_{SP}$ the bond lengths within the spin chain is modulated being alternatively shorter or longer leading to an exchange coupling stronger ($J_1 = J(1+\delta)$) or weaker ($J_1 = J(1-\delta)$) respectively. The presence of non-magnetic defects (empty circle) create finite chains. (b) If the chain contains an even number of spin, they form pairs and the ground state is non-magnetic but (c) if it contains an odd number of spins, one spin remained unpaired and the ground state is magnetic. (d) Local magnetization of the chin in (c) calculated by DMRG [34] with δ=0.1.

of the structure along the chain axis. To describe the systems in the spin-Peierls phase we will use the $S = \frac{1}{2}$ alternating-exchange Heisenberg chain Hamiltonian.

$$\mathcal{H} = \sum_i [J(1+\delta)\boldsymbol{S}_{2i-1} \cdot \boldsymbol{S}_{2i} + J(1-\delta)\boldsymbol{S}_{2i} \cdot \boldsymbol{S}_{2i+1}] \quad . \tag{1}$$

Here $J > 0$ is the AFM isotropic Heisenberg exchange integral and δ the explicit alternation parameter. In a spin-Peierls system, δ is related to the elastic energy of the lattice and the magneto-elastic coupling, which are both responsible for the dimerization of the chain. The effects of impurities in quantum spin chains have been actively studied in the past. Thanks to the improvement of numerical methods, studies using exact diagonalization [30], Quantum Monte Carlo [31, 32] and Density Matrix Renormalization Group [33] exhibit the many-body nature of non-magnetic defects.

Fig. 2 summarizes the spin-Peierls transition and the effect of non-magnetic impurities. In the case of a finite length dimerized chain, parity plays an important role in determining the magnetic properties. In case of an even number of spins (Fig.2(b)), they create pairs of spins and the ground state is non-magnetic with a large gap comparable to that of the infinite spin-Peierls chain. In case of an odd number of spins (Fig.2(c)), one spin remains unpaired and the ground state is magnetic, separated from the next states by a gap comparable to that of the infinite chain. However, contrary to a magnetic impurity inside a non-magnetic medium [35], the unpaired spin is correlated to the rest of the chain and the local polarization is spread over many neighbor spins, forming a magnetic soliton (as calculated by DMRG [34] with δ=0.1 Fig.2(d)).

Since the ground state of the spin chain defects is a doublet of effective spin $S = \frac{1}{2}$ it should be quantitatively accessible through temperature dependent static susceptibility by means of SQUID magnetometry or electron spin resonance (ESR). The former method suffers from the impossibility to separate the effect of spin chain defects from other extrinsic contribution (dirt, paramagnetic impurities...). ESR, by adding the spectral dimension, can separate the different contributions.

In this paper we present an ESR investigation of $(o\text{-DMTTF})_2X$ with X=Cl, Br and I from room temperature down to $T = 5$ K. ESR measurements on these systems have been reported [12, 14], but with a weak density of data points and, as we will explain in the following, an incorrect analysis of the gap. First, in Sec. III A we present the magnetic susceptibility and extract a quantitative estimation of the microscopic parameters, such as the temperature dependence of the intra-chain coupling $J_{eff}(T)$ (Sec. III A 1), the temperature dependence of the dimerization parameter and the gap across the spin-Peierls transition(Sec. III A 2), and the content of spin chain defects. Then, in Sec. III B by means of a continuous wave (CW) and pulsed ESR we study the dynamics of isolated and coupled magnetic solitons pinned

by non-magnetic defects of the chain.

II. EXPERIMENTAL DETAILS

Single crystals of (o-DMTTF)$_2$Br, (o-DMTTF)$_2$I and (o-DMTTF)$_2$Cl have been grown by electrocrystallization using the standard procedure described in Ref. [26]. The crystals are needle shape with the chain axis along the long length of the needle. The largest crystals have been used in the low temperature ESR study where the signal of the defects are observed but weak due to the low concentration of strongly correlated defects. The typical size was 0.2×0.2×3 mm^3 along the a, b and c axes. To avoid effects of temperature cycle history, a fresh sample was used for each series of measurements. The samples were glued on suprasil quartz rode using a small amount of Apiezon grease on one side of the samples to avoid too much stress while sweeping the temperature.

CW-ESR measurements were performed using a conventional Bruker EMX spectrometer operating in X-band with microwave frequencies of about $f_{mw} = 9.387$ GHz. This spectrometer is equipped with a He-flow cryostat (ESR900) and a cryogen-free cooler (Bruker Stinger)which operates down to 7 K. The angular dependence of ESR with respect to the static field was measured using an automatic goniometer installed on the spectrometer. The angle $\theta = 0°$ corresponds to $H \| c$. We paid particular attention to the low temperature regime where the relaxation could be long. Therefore, the microwave power was set low (< 1 mW) to prevent the ESR signal from saturation. The field modulation was set under 1 G to avoid the distortion of ESR lines due to over-modulation effect.

For pulsed ESR experiments, we used a Bruker Elexsys E580 spectrometer equipped with a cryogen-free cryostat. The Rabi oscillation measurements were performed with the external static field H_0 applied along the c-axis and the microwave frequency of $f_{mw} = 9.693$ GHz.The amplitude of the microwave field h_{mw} was calibrated using a $S = \frac{1}{2}$ radical. The sequence used was the following: $p(t) - T - \pi/2 - \tau - \pi$-echo, with $p(t)$ the Rabi pulse of a duration t, $T \gg T_2$ the waiting time and $\pi/2 - \tau - \pi$-echo is the standard Hahn echo used to probe $\langle S_z \rangle (t)$. A $S = \frac{1}{2}$ radical (DPPH) is used to calibrate the amplitude of the microwave field.

III. RESULTS AND DISCUSSION

A. Susceptibility

Let us first describe the magnetic susceptibility extracted from ESR measurements. In the linear response theory, the susceptibility from ESR χ_s is usually related to the spectral intensity using the Kramers Krönig relation: $\chi_s = \int \chi"(\omega) d\omega$ which in case of small linewidth and anisotropy becomes $\chi_s = \int I_{ESR}(H) dH$. This is true when the ESR signal is due to absorption only, but here, (o-DMTTF)$_2X$ is a conductor at high temperature and the dispersion induced by the conductivity has to be taken into account [36]. We use eq.(S1) to fit our ESR data:

$$I_{ESR} = A \left(\frac{\Gamma \cos\phi}{\Gamma^2 + (H - H_0)^2} + \frac{(H - H_0)\sin\phi}{\Gamma^2 + (H - H_0)^2} \right) \quad (2)$$

where A is the amplitude of the signal and is directly proportional to the magnetic susceptibility, Γ is half-width at half-maximum, H_0 is the resonance field and ϕ the angle of dispersion. This fit procedure is very accurate for all orientations and for T>20 K. However below 20 K the signal attributed to the spin chain defects cannot be fitted by eq. (S1) with a good accuracy and we decided to use the standard double integration of the signal to obtain χ_s. This is possible since at these temperatures the (o-DMTTF)$_2X$ family is an insulator [27].

Fig.3 (a) shows the temperature dependence of the susceptibility extracted from the ESR measurements $\chi_{ESR}(T)$ of (o-DMTTF)$_2$I and (o-DMTTF)$_2$Br ((o-DMTTF)$_2$Cl is very close to (o-DMTTF)$_2$Br and is reported in the *Supplementary Materials* [37] to avoid overloading of Fig.3). χ_{ESR} is usually in arbitrary units since it depends on the experimental parameters. However, using reference data, it is possible to renormalize χ_{ESR} to absolute units. In our case, we renormalized χ_{ESR} using independent SQUID measurements of the same compounds [27]. In Fig. 3, the squares and circles are ESR data while the lines are SQUID measurements from Ref.[27]. Above T_{SP} the susceptibilities measured by ESR and by the SQUID are very similar. However, at low temperature the Curie tails induces by magnetic impurities are clearly different.

Table I. Concentration of $S = 1/2$ defects extracted from the Curie like behavior at low temperature assuming g=2

	SQUID $10^{-4}.at^{-1}$ [27]	ESR $10^{-4}.at^{-1}$
(o-DMTTF)$_2$Cl	25	5.6
(o-DMTTF)$_2$Br	37	6.6
(o-DMTTF)$_2$I	14	4

Table I shows the concentration of defects/impurities extracted from the Curie behavior at low temperature assuming $S = 1/2$ and g=2. Clearly, the quantity of impurities is larger in the SQUID measurements than in ESR. This is not surprising since SQUID measurements are not selective and yield the total magnetic moment of a bulk sample, while ESR is highly selective and provides information on a particular kind of impurities. Fig. 3(b) shows the spin chain susctibility χ_c upon the deduction of the low-temperature Curie-tails. For the full range of temperature and in the limit of experimental error, the

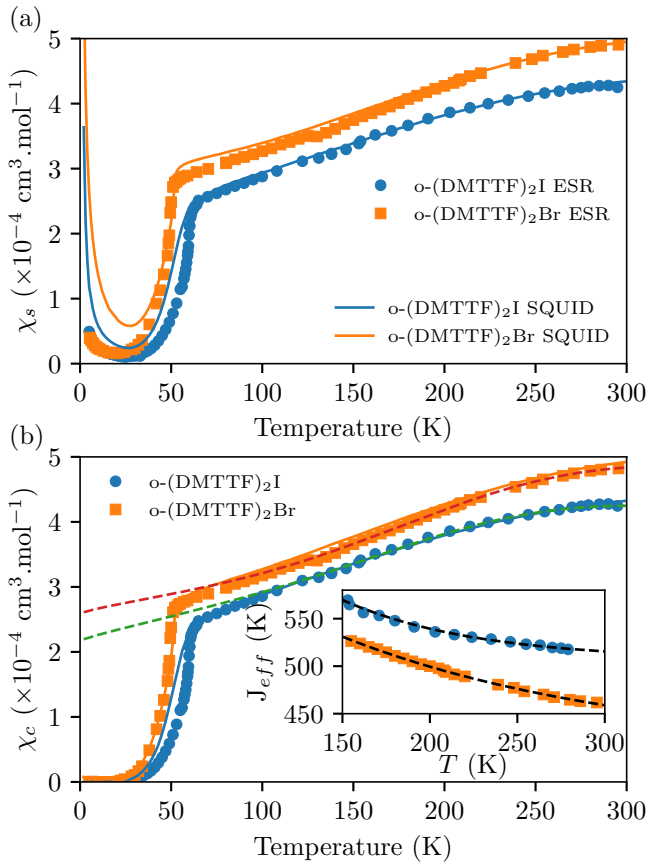

Figure 3. (a) Temperature dependence of the spin susceptibility χ_s deduced from ESR in (o-DMTTF)$_2$Br (squares) and (o-DMTTF)$_2$I (circles). The plain lines are SQUID data adapted from ref [27]. (b) Temperature dependence of the spin susceptibility corrected for the Curie tail of $S = 1/2$ defects χ_c (see table I). The dashed lines are the theoretical values of the susceptibility using exchange constants J_{eff} presented in the inset and extrapolated to low temperature.

SQUID and ESR data on (o-DMTTF)$_2$Br are identical. This is less clear for (o-DMTTF)$_2$I. For $T > T_{SP}$ SQUID and ESR susceptibility are identical, however, below T_{SP}, χ_c from ESR shows a much stronger temperature dependence than the SQUID one. We think that this difference is due to the nature of (o-DMTTF)$_2$I which should be close to a highly pressure-sensitive region of the phase diagram. As noted in Ref. [27] (o-DMTTF)$_2$I is difficult to place on the phase diagram. The authors observed a charge density wave (CDW) transition at $T_C = 47$ K and no gap in the ESR indicating a position in the high-pressure zone of the phase diagram, while we observe a clear spin-Peierls transition at T_{SP} =63 K and a behavior comparable to that of (o-DMTTF)$_2$Br and (o-DMTTF)$_2$Cl suggesting a pressure lower than expected. This difference might be due to the method of gluing the samples, which can induce different strains at low temperature.

In the following we describe the susceptibility in both the uniform spin chain phase ($T > T_{SP}$) and the dimerized phase ($T < T_{SP}$) using a method developed by Johnston *et al.* [38]. My means of Quantum Monte Carlo (QMC) and transfer-matrix density-matrix renormalization group (TMRG) they unified and improved the theoretical predictions developed for the dimerized spin chain by Bulaevskii [39] and for the uniform spin chain by Bonner and Fisher [40], Eggert Affleck and Takahashi [41], and Klümper and Johnston [42] .

1. *Uniform chain susceptibility*

In the uniform spin chain regime ($T > T_{SP}$), all the models cited above failed to describe the susceptibility of (o-DMTTF)$_2X$. This anomaly has been observed in (TMTTF)$_2$PF$_6$ [43], deuterated (TMTTF)$_2$PF$_6$D$_{12}$[44], (TMTTF)$_2$SbF$_6$[5],(TMTTF)$_2$AsF$_6$ [45] and has been attributed to thermal expansion. All the theoretical models describe susceptibility at constant volume ($[\chi]_V$) while measurements are performed at constant pressure ($[\chi]_P$). A method to convert the temperature dependence of ($[\chi]_P$) to ($[\chi]_V$) was developed by Wzietek *et al.* [46] in the case of (TMTSF)$_2$PF$_6$ by performing X-ray and nuclear magnetic resonance (NMR) under pressure. This method is laborious and suffers from the arbitrarity of choice of reference temperature volume. We choose a different approach by extracting the exchange constant J as function of the temperature at constant pressure. This is possible with the Johnston *et al.* method but needs very accurate absolute measurements.

To describe the uniform spin chain phase we use the following method: (a) we choose a range of temperature far enough from T_{SP} to avoid fluctuations of spin-Peierls and ensure that the alternating parameter δ vanishes, in our case T=150 K to 300 K, which is at least 3 times T_{SP}. (b) We use the Padé approximant and the coefficients provided in Table I of Ref.[38] to extract the exchange constant $J_{eff}(T)$ for each temperature in this range. The result is provided in the inset of Fig.3(b) for (o-DMTTF)$_2$Br and (o-DMTTF)$_2$I. We observe that the effective exchange coupling J_{eff} decreases as T increases. Such behavior has been noticed in NaV_2O_5 [38] and qualitatively explained by Sandvik *et al.* [47] and Kühne *et al.* [48] by including dispersionless phonons (Einstein phonons) linearly coupled to the spin chain. In our case, a more direct effect is the variation of cell volume observed by changing the temperature. Radical organic salts are known to have a large thermal expansion compared to inorganic metal oxides. In (TMTYF)$_2$XF$_6$ (with X=Sb, As, P and Y=S or Se)[49–51] the variation of the chain length is about 3%. For (o-DMTTF)$_2$Br and (o-DMTTF)$_2$I, the X-ray diffraction measurements show a linear temperature dependence of the cell parameters, theincrase of c change between $T = 100$ K and room temperature of about 2% (see Appendix A for details).

To estimate the effect of the variation of the cell parameter c, we used the molecular DFT calculation on a

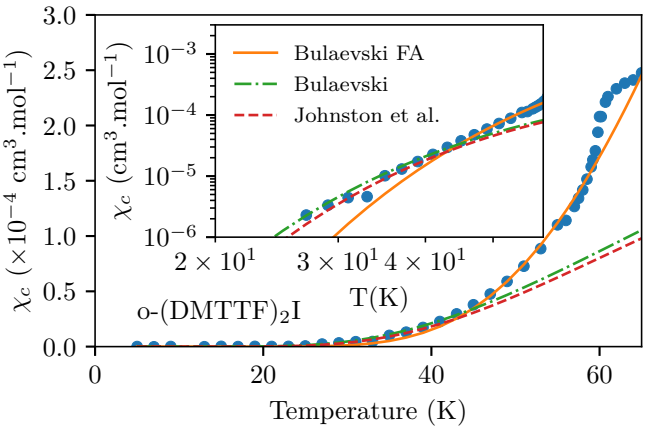

Figure 4. Temperature dependence of the spin susceptibility in the low-temperature region for (o-DMTTF)$_2$I. Below T_{SP} =63 K the susceptibility drops to the non-magnetic spin-Peierls state. The plain orange line is the best fit using eq. (3) taking α and Δ as two independent fit parameters. The green dashed dot and red dashed lines are the best fits to the Bulaevski and Johnston *et al.* model respectively using only δ as a fit parameter. The inset is the log-log scale of the figure, magnifying the discrepancy of the Bulaeveski FA model at low temperature. Analysis for (o-DMTTF)$_2$Br and (o-DMTTF)$_2$Cl are provided in [37]

minimal dimer cell (see Appendix B). A 2% change of the distance between 2 o-(DMTTF)$_2$ molecules leads to 13% change of the exchange constant, in agreement with the values of J_{eff} presented in the inset of Fig.3(b)

By incorporating the effective exchange coupling constant J_{eff} calculated from $T = 150$ K to $T = 300$ K and extrapolated to lower temperature into the uniform spin chain model [52] we obtain the colored dashed lines in Fig. 3(b). We notice that susceptibility calculated using the extrapolated J_{eff} reproduces the experimental data with a good accuracy down to $T = 100$ K. A small discrepancy observed for $T < 100$ K can be attributed to the opening of a pseudogap, which is in agreement with the temperature where weak diffuse X-ray scattering lines were observed [27]- a sign of a pretransitional effect.

2. *Dimerization of the spin chain*

For $T < T_{SP}$ the gapless Heisenberg uniform spin chain progressively enters in a non-magnetic gapped stated ($S = 0$) via a spin-Peierls transition [27]. The susceptibility extracted from our ESR study (χ_{ESR}) below T_{SP} shows no significant difference from the DC susceptibility from previous SQUID measurements for either (o-DMTTF)$_2$Br (Fig. 3) or (o-DMTTF)$_2$Cl (see SI). However, for (o-DMTTF)$_2$I shows a temperature dependence comparable to that in (o-DMTTF)$_2$Br and (o-DMTTF)$_2$Cl (with a higher T_{SP}) but is significantly different from the SQUID data.

The determination of the spin gap Δ is of fundamental importance since it is directly related to the dimerization parameter δ [53, 54]. However it is a tricky problem since it depends on the microscopic model used. The model that is the most widely used in the literature was developed by Bulaevski [39] and consists in the analytical calculation of the susceptibility in the Hartree-Fock approximation. He calculated the magnon dispersion of coupled dimers and in the low temperature approximation he provided a simple two-parameter form of the susceptibility:

$$\chi_s(T) = \frac{\mathcal{N}_a g^2 \mu_B^2}{k_B T}.\alpha(\delta) \exp\left(-\frac{\Delta_B(\delta) J_1}{k_B T}\right) \qquad (3)$$

With $J_1 = J(1+\delta)$, in cgs units and with $g \approx 2$ the pre-factor is close to 0.375. α is the amplitude factor and $\Delta_B.J_1$ is the gap.Despite its simplicity, this model shows remarkably good agreement with modern numerical approach for large dimerization ($\delta > 0.5$)[38, 53] but the agreement becomes progressively worse as δ decreases and break down for $\delta < 0.1$. In the latter case, the reason is that the magnon dispersion minimum is not at $k = 0$ [53]. Independently of the range of validity of δ in the Bulaevski's model, one should use eq. (3) with caution. First of all, Bulaevski's approach is essentially a low-temperature one; the dimerization parameter δ and the energy gap Δ are independent of temperature. This is, of course, not fulfilled in the entire range of existence of the spin-Peierls state. Orignac *et al.* [55] showed that $\Delta(T) = \Delta(0)$ for $T < 0.5T_{SP}$. The second point to take care of is that the two parameters α (the amplitude) and Δ (the spin gap) are not independent. Rather, both are functions of δ, tabulated in Ref. [37, 39]. The latter fact has been often neglected, leading to an incorrect use of the Bulaevski model [14, 43, 56].

An example of determination of the dimerization parameter δ by different methods using χ_{ESR} for (o-DMTTF)$_2$I is given in Fig. 4. The model labeled "Bulaevski free amplitude (Bul. FA)" corresponds to eq. (3) with $\alpha(\delta)$ replaced by α, which is now a free parameter independent of δ, while $\Delta_B(\delta)$ remains a function of δ. It is clear that this model is incorrect and should not be used but it was applied in the past to extract the dimerization parameter of spin-Peierls systems[12, 43, 57] and had certainly provided an overestimated δ as we will se in the following. The fit labeled "Bulaevski" is eq. (3) with only δ as a free parameter as it should be used. Finally, "Johnston *et al.* " is a direct numerical calculation of the susceptibility using TMRG with only δ as a free parameter. "Johnston *et al.* " use the Padé approximant and the coefficients provided in Table I of Ref.[38] and does not suffer of the approximation made by Bulaevski for his analytical description (3) At first sight Bul. FA seems a better fit, but a closer look at low temperature on the log-log scale (Fig. 4 inset) detects an important discrepancy with the data. On the contrary, the two other models used, correctly show a very good agreement with experimental data for $T < 40$ K. At higher temperature

the dimerization $\delta(T)$ decreases and the models cannot be used in the current form any more.

Table II. Dimerimzation parameter $\delta(T=0)$ extracted from three different models: Bulaevski free amplitude (Bul. FA) correspond to eq. (3) with α left as a free parameter, Bulaevski model is (3) with δ is the only fit parameter and the Johnston *et al.* model. (see text for details)

	Bul. FA	Bulaevski [39]	Johnston *et al.* [38]
(o-DMTTF)$_2$Cl	0.17	0.088	0.083
(o-DMTTF)$_2$Br	0.14	0.085	0.080
(o-DMTTF)$_2$I	0.18	0.10	0.096

Let us note a large overestimation of δ in the Bul. FA fit while Bulaevski and Johnston *et al.* fits produce rather consistent values of δ, those of Bulaevski being slightly higher.

The relation between the magnetic gap Δ and the dimerization parameter δ is a central problem in understanding the microscopic properties of dimerized spin chains. It has been intensively studied in the past, following the development of modern analytical (like bosonization) or numerical (DMRG) approaches. It was shown [58] that the critical behavior $\Delta \sim \delta^{2/3}$ [59] must be corrected to $\Delta \sim \delta^{2/3}/|\ln\delta|^{1/2}$ [60]. Note the absence of prefactors in the early developments in the field. More recently numerical developments have led to quantitative description of the spin gap, like $\Delta/J = 2\delta^{3/4}$ by Barnes *et al.* [53], $\Delta/J = 1.94\delta^{0.73}$ by Papenbrock *et al.* [61], and the elegant analytical solution proposed by Orignac [62] $\Delta/J = 1.723\delta^{2/3}$. The validity of all these formulas depends on the range of δ, for $\delta \sim 0.1$ the agreement lies within 5%.

The particularity of spin-Peierls systems is to have a temperature-dependent gap. Far below the transition temperature the gap is independent of temperature and the method presented above is sufficient to estimate Δ. However, for $0.5T_{SP} \lesssim T < T_{SP}$ the gap has to be treated more carefully. Here we treat the temperature dependence of the spin gap $\Delta(T)$ following Johnston *et al.* [38]. Proceeding from the temperature dependence of the exchange constant found in III A 1, see the inset of Fig. 3(b), we extrapolate $J_{eff}(T)$ towards lower temperatures and evaluate it just above $T_{\rm SP}$. Let us denote this value by J^*_{SP}). We obtain $J^*_{SP} \simeq 600$ K for (o-DMTTF)$_2$Cl and (o-DMTTF)$_2$Br and $J^*_{SP} \simeq 670$ K for (o-DMTTF)$_2$I. Then $\delta(T)$ is computed using the fit function for the alternating-exchange chain (see Table II of Ref. 38) by finding the root for δ at each experimental point. Finally, the temperature dependence of the spin gap Δ(T) is computed using the Barnes *et al.* [53] relation, $\Delta(T) = 2\delta^{3/4}J^*_{SP}$.

The temperature dependence of the alternation parameter $\delta(T)$ and the corresponding spin gap $\Delta(T)$ for (o-DMTTF)$_2$I, (o-DMTTF)$_2$Br and (o-DMTTF)$_2$Cl is given in Fig. 5. The method used to extract $\delta(T)$ is explained in Ref.[38] and summarized here: for each value of the susceptibility $\chi_c(T)$ we solve the equation $\chi_J(\delta, J, T) = \chi_c(T)$ for non-vanishing value of χ_c. Where $\chi_J(\delta, J, T)$ is the susceptibility provided by the Johnston *et al.* model. Knowing J from the Sec. III A 1 we obtain δ as function of temperature. The dashed lines correspond to the values of δ and Δ at $T = 0$ K taken from Fig. 4 and Tab. II. We notice that for $T < 0.75T_{SP}$ the dashed lines are the asymptotes of $\delta(T)$ and $\Delta(T)$. It is worthwhile noticing that the method described above is valid when the susceptibility is non zero. This is the reason why no value can be provided below about 25 K. We show that below $0.75T_{\rm SP}$, δ and Δ are independent of temperature and can be estimated by their values at $T = 0$ K values. Above $0.75T_{\rm SP}$ the dimerization parameter $\delta(T)$ and the spin gap $\Delta(T)$ decrease as T approaches $T_{\rm SP}$, but they do not vanish at $T = T_{\rm SP}$. The data in Fig.

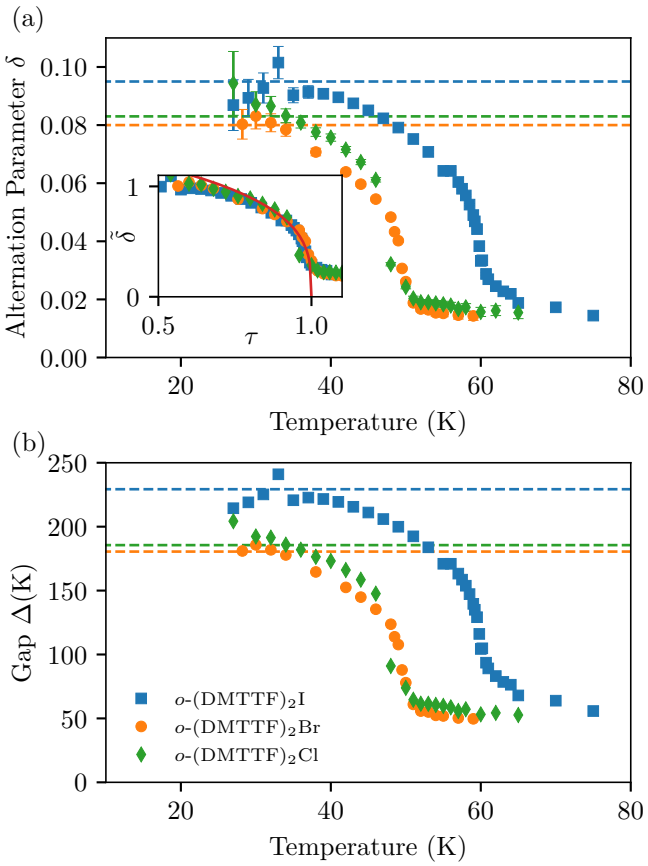

Figure 5. Temperature dependence of (a) the dimerization parameter δ and (b) the spin gap Δ for (o-DMTTF)$_2$I (blue squares), (o-DMTTF)$_2$Br (orange circles) and (o-DMTTF)$_2$Cl (green diamonds). The dashed lines represent the values estimated at $T = 0$ K (see Table II). The inset is the reduced temperature dependence ($\tau = T/T_{SP}$) of the reduced dimerization parameter $\tilde{\delta} = \delta(T)/\delta(0)$.

5 clearly show the existence of spin dimerization fluctuations and a spin pseudogap above T_{SP} for the three (o-DMTTF)$_2X$ compounds of about 20% and 30% of $\delta(0)$ and $\Delta(0)$, respectively. The fluctuation effects above T_{SP} seem to persist at high temperature and show a pretransitional effect of the lattice confirming the observation reported by X-ray diffusion scattering [27]. Precursor effects above T_{SP} have been reported in both organic [63] and inorganic [64, 65] spin-Peierls systems. Fig. 5(a) inset shows the variation of the reduced dimerization parameter $\tilde{\delta} = \delta(T)/\delta(0)$ as function of the reduced temperature $\tau = T/T_{SP}$. Once renormalized, the dimerization parameters of (o-DMTTF)$_2$Cl, (o-DMTTF)$_2$Br and (o-DMTTF)$_2$I present a universal thermal behavior.

Using the Barnes *et al.* formula [53], the temperature dependence of δ, and the exchange coupling at low temperature J^*_{SP}, we calculate the temperature dependence of the gap (see Fig. 5(b)). Above T_{SP} a pseudo-gap of about 50 K is clearly visible and tend to reduce as T increases. Below T_{SP} the gaps open up and become temperature-independent below $0.75T_{SP}$, reaching 180 K for (o-DMTTF)$_2$Cl and (o-DMTTF)$_2$Br and 230 K for (o-DMTTF)$_2$I.

B. Electronic Interaction

Let us now turn to the discussion of the low-temperature behavior. When the systems enter in the spin-Peierls phase, the tetramerization of the DMTTF molecule stacks occurs. We have shown above that this transition is continuous. Below about $T_{SP}/2$ (o-DMTTF)$_2X$ can be considered stabilized since the Δ and δ are temperature independent. In a perfect and infinite system, the ground state is non-magnetic ($S = 0$) and no ESR signal should be observed. However in the section III A we have shown the existence of a weak signal corresponding to some 10^{-4}.at^{-1} impurities. One of the strengths of ESR is the possibility to separate the magnetic contribution (extrinsic or intrinsic) and it was shown in previous studies[12–14] that the ESR signal observed at very low temperature comes from spin chain defects. By itself, the defect is non-magnetic and is a break in the transnational symmetry like a chain-end or a stacking fault of the alternation parameter. These topological defects were extensively studied theoretically[8, 9, 30, 66, 67] and observed by magnetometry[68], NMR [69] and EPR [13, 70, 71].

ESR signal of the defects in (o-DMTTF)$_2$Br is presented in Fig. 6(a). It is recorded at $T = 5$ K, which is far below T_{SP}. The signal contains the expected line of the spin chain defect as it was reported previously [12, 72], but more surprisingly, one can clearly see two shoulders on both sides of the central line. The satellite signal is only visible in (o-DMTTF)$_2$Br. To separate and quantify the different contributions, we used to following procedure:

The blue line is the best fit using the derivative of a Lorentzian eq. (S1) of the central line. To get an accurate fit of the central line, the points close to the shoulders have been removed from the fit procedure. Then, we have subtracted this fit, in order to remove the contribution of the central line from the original ESR signal. This method shows with a good accuracy the position of the satellite lines (black arrows) since the central line does not perturb anymore the position of the satellites. The angular dependence of the g-factor of the central line is reported in figure Fig.6(b). For comparison, the g-factor anisotropy of the uniform spin chain measured at room temperature is also presented. The angular dependence of the g factor can be well described by the following relation for a g tensor with uniaxial symmetry.

$$g(\theta) = \sqrt{g_{\parallel}^2 \cos^2\theta + g_{\perp}^2 \sin^2\theta} \quad , \tag{4}$$

Within the error limit of 10^{-5} the g tensors at both temperatures are identical. However, it is important to notice that the low temperature signal cannot be attributed to the infinite chain, which is fully dimerized at this temperature, but is rather attributed to defects in the dimerized chain. The same angular dependence is observed in (o-DMTTF)$_2$Cl and (o-DMTTF)$_2$I.

The presence of the satellite lines is more intriguing. Such a structure is often attributed to the triplet signal [71, 73] of the dimer but this should be visible at a temperature close to the gap. However here we are at a much lower temperature and the excited state of the infinite spin-Peierls chain must be depopulated: at $T = 5$ K the relative content of spins in the first excited state for $\Delta_{Br} = 180$ K is 10^{-16} (see Fig. 5). As a consequence, we can exclude that the satellites come from the excited state of the spin-Peierls chains.

The angular dependence of the satellites in (o-DMTTF)$_2$Br is presented in Fig. 7. Fig. 7(a) shows a series of fit residues obtained by the method presented in Fig. 6(a). The circles present the resonance field of the central line. We can see that the center of gravity of the satellites follows the angular dependence of the central line (circles). As a consequence, the satellite signal is related to the defects of the spin chains. Using the well resolved angular dependence of the satellite signals of (o-DMTTF)$_2$Br, we extract the line separation as a function of the static field orientation (Fig. 7(b)). The error bars are due to the difficult fitting of the central line when the satellites are not clearly resolved as it is the case near the magic angle ($\sim 54°$). The data in Fig. 7(b) are fitted to an Ising-like anisotropy expression, $d(3\cos^2\theta - 1)$, with $d = 4.2 \pm 0.3$ G. It important to mention that the satellite signal was not resolved for (o-DMTTF)$_2$Cl at any angle but the linewidth of the central lines have shown the same anisotropy at low temperature [14]. Moreover the satellites were not reported in [14], certainly because of saturation which prevented them for being resolved. Intriguingly, neither the satellites nor a clear linewidth anisotropy is observed in (o-DMTTF)$_2$I.

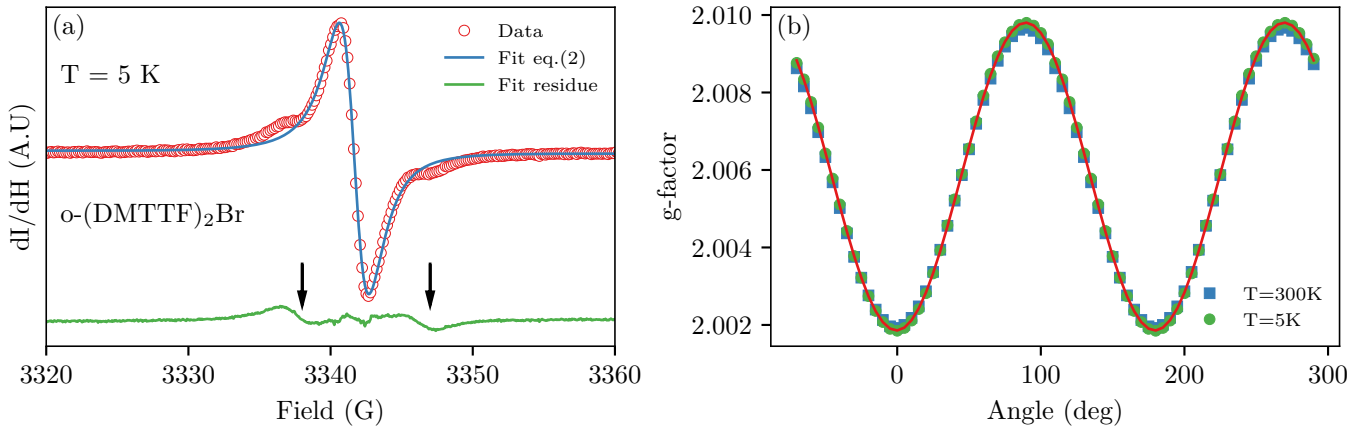

Figure 6. (a) Example of ESR signal of (o-DMTTF)$_2$Br at $T = 5$ K and magnetic field $H\|c$. The central line has been fitted using a derivative of a lorenzian (blue line). The residue of the fit is presented by the green line where the arrows point the two satellite signals. (b) Angular dependence of the g-factor of the central line of defects in the spin chain measured at $T = 5$ K and of the uniform spin chain line measured at $T = 300$ K. The green line is the best fit using eq. (4) with $g_{\|} = 2.0019$ and $g_{\perp} = 2.0098$

Such angular dependence can be attributed to a dipole-dipole interaction between chain defects or to a $S = 1$ entity like a triplon (singlet-triplet excitation) which is split by an axial anisotropy. A pair of spins of chain defects coming from the random distribution of the disorder is unlikely. Indeed, the probability to find a pair of impurities with the concentration reported in Tab. I is very small. For example, using the concentration of defects in (o-DMTTF)$_2$Br (6.6×10^{-4}) and assuming a simple cubic lattice, the probability of finding a random pair is 3.9×10^{-4} [74] while the intensity of ESR signal of the satellites leads to a probability of nearly 3 orders of magnitude bigger. Random pair defects were recently observed by ESR on the quasi-two-dimensional organic (BEDT-TTF)$_2$Cu[N(CN)$_2$]I [75] but the concentration of defects were substantially higher (1%) which leads to a probability of pair existence of 5%.

Another explanation comes directly from the 1D nature of (o-DMTTF)$_2X$. Fig. 8 shows the local structure of spins induced by a break in the translational symmetry (empty circle). We consider only chains with a non-dimerized spin spins on the left-hand side (blue spins). On the other side of the defect, there is also a chain (red spins). If the latter chain starts with a strong link ($J_1 = J(1+\delta)$), only the unpaired spin from the left side chain contribute to the signal. However, if the right side chain starts with a weak link ($J_2 = J(1-\delta)$) the unpaired spins of the two finite chains are close and can interact together with an effective coupling J$_P$. In this scenario, the probability of having a pair of interacting magnetic solitons rises to 50% of the total number of solitons and is independent of the concentration of defects [37].

To prove the triplet origin of the satellite lines we performed Rabi oscillation sequence of the ESR lines. This pulse-ESR sequence is made of 3 pulses, le first pulse induces a coherent rotation of the spins around the microwave field axis and the next 2 pulses generate a Hanh echo with an intensity proportional to the magnetization at the end of the first pulse. By adding the time dimension to each field point of the ESR line (Fig. 6)(a) it is possible to probe the nature of the spin transition even if the ESR is not resolved[76].

Fig. 9 shows the Rabi oscillations of the defect signals in (o-DMTTF)$_2$Br at $T = 5$ K and $H_0\|c$. Like in CW-ESR, the microwave frequency is fixed. Here in addition the static field H_0 is fixed during the time of the sequence. For $H_0^1 = 3458$ G the central ESR line is probed, while for $H_0^2 = 3454$ G we probe one of the satellite lines. The two lines have clearly different dynamics. For H_0^1 (H_0^2), the microwave field amplitude dependence is presented in the inset with red circles (blue squares). The dashed line is the Rabi frequency dependence expected for a spin $S = 1/2$ and the dashed dot line for the one of a spin $S = 1$ using the equation [77]:

$$\nu_R^{S=1} = \sqrt{S(S+1) - S_z(S_z+1)} \times \nu_R^{S=1/2} \quad . \qquad (5)$$

S_z is the level in which the Rabi oscillation starts, for $S = 1/2$, $S_z = -1/2$ and for $S = 1$, $S_z = -1$ and 0. In the absence of a fit parameter, we found $\nu_R(H_0^2) = \sqrt{2}\nu_R(H_0^1)$ confirming the $S = 1$ nature of the satellite lines. A field sweep Rabi oscillation sequence is presented in Fig. 9(b). This figure presents the contour-plot of the Rabi frequency distribution for $H_0\|c$ and is made of the fast Fourier transform (FFT) of the Rabi oscillations obtained from Fig. 9(a) while changing the static field. The dashed (dash doted) line shows where the Rabi frequency of a spin $S = 1/2$ ($S = 1$) is expected. This method shows without ambiguity the triplet nature of the satellite lines with a slight anisotropy $d = 4$ G. In the case of no or too weak coupling between the magnetic solitons proposed in Fig. 8(b) the Rabi frequency

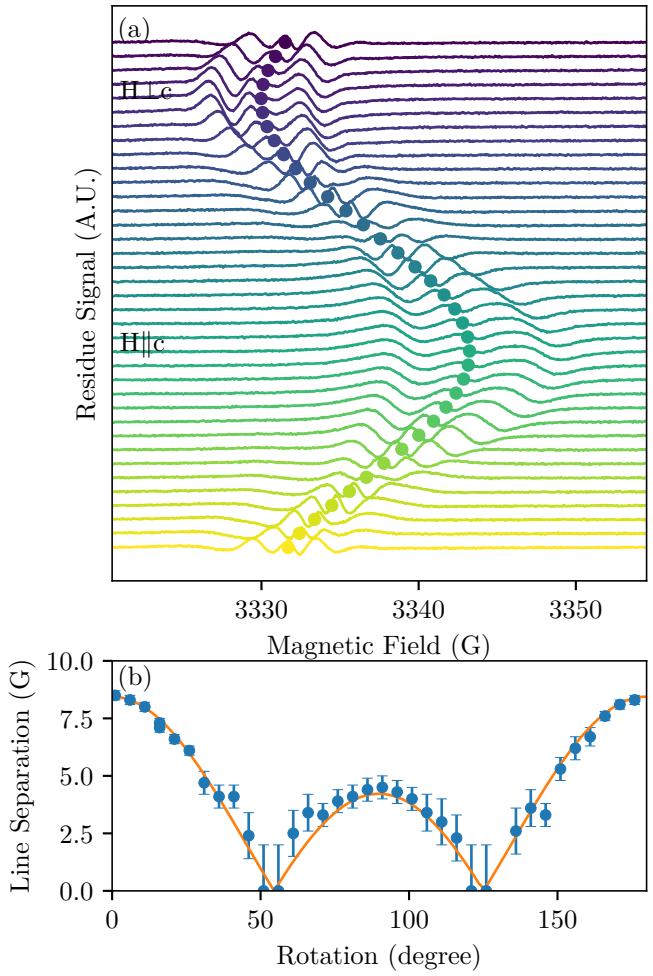

Figure 7. Angular dependence of the satellites of (o-DMTTF)$_2$Br at $T = 5$ K. (a) Angular dependence of the fit residue. The circles show the resonance field of the central line. (b) Field separation of the satellites. The plain line is the best fit to an Ising-like expression $d(3\cos^2\theta - 1)$.

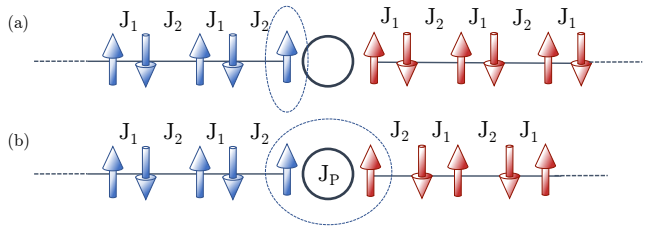

Figure 8. Schematic representation of the spin configuration around a non-magnetic defect in the middle of the chain. (a) When on one side of the defect there is an unpaired spin and on the other side the spin is paired with its neighbor, only the unpaired spin contributes to the ESR signal. (b) When on both sides of the defect the spins are unpaired, an effective coupling occurs leading to a triplon.

should have been the one for $S = \frac{1}{2}$. Let us discus the cases of (o-DMTTF)$_2$Cl and (o-DMTTF)$_2$I. CW-ESR has shown no satellite lines, no matter what the temperature and the orientation were. The field sweep Rabi oscillation measurement shows no signature of a $S = 1$ in (o-DMTTF)$_2$I but exhibits the Rabi frequency mode of $S = 1$ for (o-DMTTF)$_2$Cl (see SI). In the latter the ESR satellite lines are unresolved in the field dimension (this is the reason why they were undetected by CW-ESR) but are resolved in the frequency dimension (see Supplementary Materials [37]).This confirms the presence of a triplon state in (o-DMTTF)$_2$Cl, assumed in Ref. [14]. It is intriguing that (o-DMTTF)$_2$I has shown no sign of paired solitons, contrary to (o-DMTTF)$_2$Br and (o-DMTTF)$_2$Cl. A possible explanation is that in (o-DMTTF)$_2$I the pinned soliton is not strictly at the end of the chain. Our model uses only explicit alternation, with no spin lattice relaxation. However, it has been shown theoretically by Hansen *et al.* [30] that if one takes the magneto-elastic coupling into account the magnetic soliton can be located either near the edges of the chain or can be repelled toward the interior. In the latter case no soliton pair can be formed.

Finally, we propose an estimation of the coupling between the pairs of magnetic solitons.

We have presented in Sec. III A an estimation of the density of defects based on the Curie law. A more sensitive presentation is provided by the product of the susceptibility with the temperature χT. In the case of the susceptibility strictly follows the Curie law, the product χT is a constant at any temperature (this is the case of (o-DMTTF)$_2$I in Fig. 10). However, if some spins $S = \frac{1}{2}$ solitons form pairs with a non-negligible coupling constant (J_P), χT is no more temperature independent. A naive description would be to simply considered 2 spins $S = \frac{1}{2}$ coupled by exchange J_P. In this case the susceptibility is described by the Bleaney and Bowers equation [78]. However the microscopic structure and the N-body nature of the soliton pairs presented in Fig. 8 is more complex and necessitates DMRG and QMC calculations, briefly described in Appendic C. It appears that the energy spectrum of a pair of solitons is made of a singlet (S=0) ground state separated from the first excited state (triplet S=1) by a small gap Δ_S and then the quasi continuum by a large gap Δ. If $T \ll \Delta$ we can consider only the low lying levels : singlet-triplet. The difference with the trivial case of two coupled spins is that the gap is no more the direct coupling between the two neighbor-spins but is renormalized by the exchange couplings in the chain. QMC shows that at low enough temperature, the susceptibility of the soliton pair can be described by the Bleaney and Bowers formula including the gap Δ_S and DMRG calculations show that $\Delta_S = 0.35 J_P$.

Consequently, we fit $\chi_{tot}T$ for (o-DMTTF)$_2$Br and (o-DMTTF)$_2$Cl using a weighted sum of a single and paired solitons:

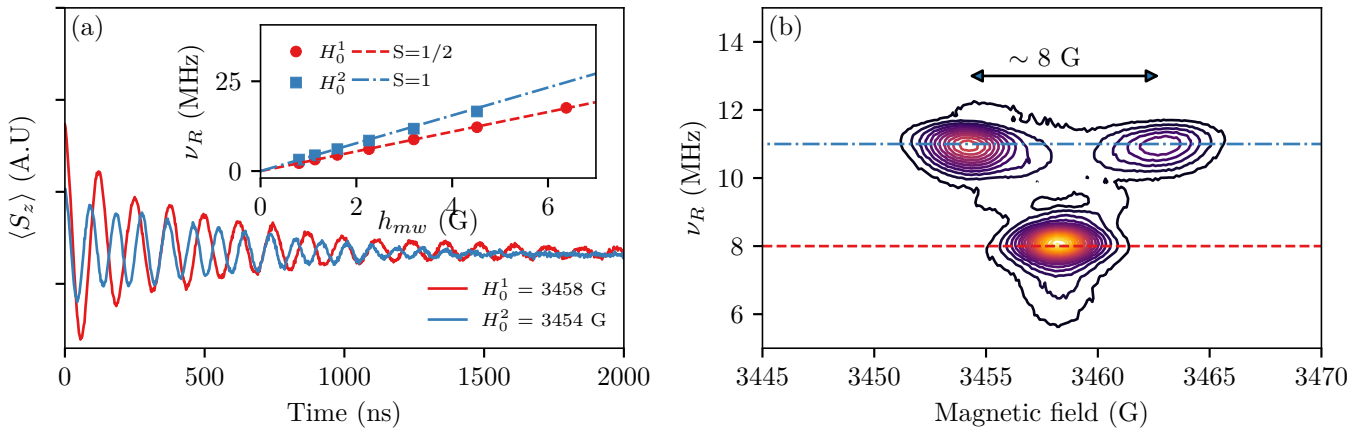

Figure 9. (a) Rabi oscillations of the strongly correlated defects of (o-DMTTF)$_2$Br at $T = 5$ K and $H_0 \| c$. The microwave frequency is fixed and the field is set at $H_0^1 = 3458$ G corresponding to the central line or $H_0^2 = 3454$ G to probe the first satellite line. The inset is the microwave field dependence of Rabi frequencies within dashed red and dash dotted blue the dependence expected for $S = \frac{1}{2}$ and $S = 1$, respectively. (b) Contour-plot of the FFT of the Rabi oscillations obtained by the three-pulse sequence presented in the main text for $H_0 \| c$.

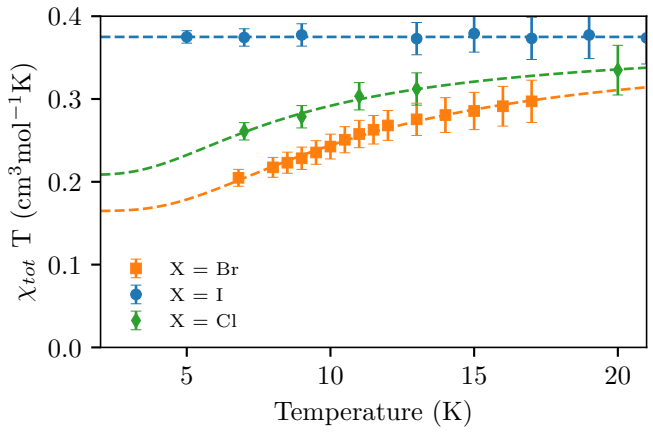

Figure 10. Product χT as function of the temperature for the three systems X=Br, I and Cl, obtained from cw-ESR measurements with $H \| c$. The dashed lines are the best fits to eq. (6)

$$\chi T = \left[\frac{n}{2\left(1 + \frac{1}{3} e^{\frac{\Delta_S}{kT}}\right)} + (1-n)\frac{3}{8} \right]. \qquad (6)$$

with χT in emu.mol^{-1}K units (in number of mole of defects) n the ratio of $S = \frac{1}{2}$ solitons forming dimers and Δ_S the gap between the singlet and the first triplet (we assume that $g = 2$ for simplicity). Fig. 10 shows the best fit using $n = 0.56$ and $\Delta_S = 20.3$ K ($J_P = 59.7$ K) for (o-DMTTF)$_2$Br and $n = 0.44$ and $\Delta_S = 16.7$ K ($J_P = 49.1$ K) for (o-DMTTF)$_2$Cl. The values of n are coherent with the model of a defect in the middle of the chain (see Fig. 8) and the effective coupling J_P is rather large and could lead to a long-distance entanglement [79].

The microscopic origin of J_P remains unclear and is beyond the scope of this article. The Ising-like anisotropy observed in Fig. 7 can be explained by two origins: (i) the symmetric anisotropic exchange interaction which is consequence to the spin orbit and can be estimated by $d = \left(\frac{\Delta g}{g}\right)^2 J_P \sim 5$ G which is in agreement with our value of d. However, it is not clear if this formula derived for uniform superexchange interaction remains valid for pairs of solitons. (ii) The direct dipole-dipole interaction: the soliton should not be treated as a point dipole but rather as a distribution of local magnetization (see Appendix C). In this way we find $d = 4.0$ G (see Sec. D for details) in good agreement with the experimental result.

IV. CONCLUSION

In conclusion, we have presented an ESR study of (o-DMTTF)$_2$Cl, (o-DMTTF)$_2$Br and (o-DMTTF)$_2$I single crystals. At low temperatures, these three compounds are organic gapped spin chains. In the high temperature regime they can be treated as isotropic Heisenberg antiferromagnetic uniform spin chains, provided that one takes into account the temperature variation of the exchange coupling due to the contraction of the crystallographic cell. We have quantified the temperature dependence of the spin gap Δ and dimerization parameter δ and shown the existence of a pseudo gap above T_{SP}. Angular and temperature dependent CW-ESR measurements have revealed the presence of magnetic solitons pinned to spin chain defects. The observation of field sweep Rabi oscillations as well as temperature dependent ESR susceptibility provides evidence of two different kinds of strongly correlated defects. These are, firstly, single magnetic solitons of spin $S = \frac{1}{2}$ in the three

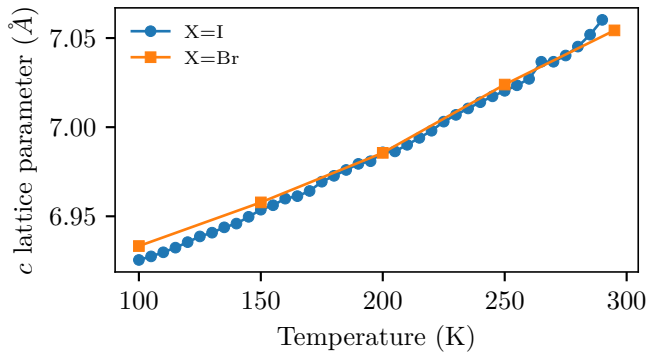

Figure 11. Temperature variation of the lattice parameter c (chain direction) for (o-DMTTF)$_2$I and (o-DMTTF)$_2$Br.

systems. Secondly,there are pairs of exchange-coupled solitons in (o-DMTTF)$_2$Br and (o-DMTTF)$_2$Cl, whose thermally activated S=1 state (triplon) is responsible for the clearly visible second Rabi frequency. Unlike in 2D and 3D media, the density of soliton pairs in a 1D system is large - about one-half of the solitons are paired - and interdependent to the concentration of defects. As a consequence, it is possible to coherently manipulate these quantum objects which could be of interest in the field of quantum information processing.

ACKNOWLEDGMENTS

This work is supported by Agence Nationale de la Recherche (ANR project "DySCORDE", ANR-20-CE29-0011). Financial support from the IR INFRANALYTICS FR2054 for conducting the research is gratefully acknowledged. We are grateful to C. Coulon for sharing the SQUID measurements used in this paper.

Appendix A: Temperature expansion of the lattice

Data collection for (o-DMTTF)$_2$I was performed on an APEXII Bruker-AXS diffractometer equipped with a CCD camera and a Cryostream 700 (Oxford Cryosystems). Sets of 3 ω-scans (6°/scan, 0.5°/frame) were taken every 5 K, the values of the unit cell parameters used are the refined values obtained after data reduction with the Bruker SMART program. Data collection for (o-DMTTF)$_2$Br was measured on a Rigaku Oxford Diffraction SuperNova diffractometer from 300 K down to 100 K every 50 K. In both systems the principal lattice variation is c, with a 2% difference between high and low temperature, while a and b change as little as 0.3% (See SI).

Appendix B: DFT Calculations

All theoretical calculations were based on the Density Functional Theory (DFT) and were performed with the ORCA program package [80]. To facilitate comparisons between theory and experiments, X-ray crystal structure of (o-DMTTF)$_2$Br was used. Our DFT molecular model was built considering two dimethetyltetrathiafulvalene units together with 8 bromine counter-ions. This model was then optimized while constraining the positions of all heavy atoms to their experimentally derived coordinates. Only the positions of the hydrogen atoms were relaxed because these are not reliably determined from the X-ray structure. Geometry optimization as well as electronic structure calculations were undertaken using the hybrid functional B3LYP [81, 82] in combination with the TZV/P [83] basis set for all atoms, and by taking advantage of the resolution of the identity (RI) approximation in the Split-RI-J variant [84] with the appropriate Coulomb fitting sets [85]. Increased integration grids (Grid4 and GridX4 in ORCA convention) and tight SCF convergence criteria were used in the calculations. In all cases, empirical dispersion corrections (D3) were included [86]. The Heisenberg isotropic exchange coupling constants J were evaluated from single point calculations based on the Broken Symmetry (BS) approach[87–89] using the B3LYP functional and the TZV/P basis set. The Yamaguchi formula[90] was used to estimate the exchange coupling constants J based on the Heisenberg–Dirac–van Vleck Hamiltonian.

We used three distances between the centers of gravity of the two (DMTTF)$_2$ molecules: 7.06Å corresponding the X-ray value at room temperature, 6.92Å corresponding the X-ray value at 100 K and a contraction of 2% (see Fig. 11) and 7.20Å corresponding to a fictitious dilatation of 2% with room temperature cell.

Table III.

	d (Å)	J_{DFT} (cm^{-1})
RX at 300K (RT)	7.06	736
RX at 100K (RT-2%)	6.92	648
Fictitious (RT+2%)	7.20	832

The exchange coupling values obtained by DFT overestimate the experimental values which is not surprising since we use a simple dimer model. It is more interesting to notice that a small variation of the inter molecular distance (here 2%) induces a variation of about 13% of J_{DFT} as observed experimentally.

Appendix C: DMRG and QMC

In order to explain the electron spins interactions in the spin-Peierls phase we perform Density Matrix Renormalization Group (DMRG) and Quantum Monte Carlo (QMC) simulations using the python ALPS toolkit [34]. We consider two magnetic structures corresponding to the model presented in Fig.8 : (i) two dimerized 31-spin chains linked by J_P and (ii) one dimerized 31-spin chain linked by J_P to a dimerized 32-spin chain, represented, respectively, by H_{SP}^{62} and H_{SP}^{63}. In all calculations we use the alternation parameter $\delta = 0.08$ (close to the experimental value Tab. II) and the exchange coupling J = 1.

$$H_{SP}^{62} = \sum_{i=-1}^{-15} [J(1+\delta)S_{2i-1}.S_{2i} + J(1-\delta)S_{2i}.S_{2i+1}] + J_P S_{-1}.S_{+1} + \sum_{i=1}^{15} [J(1-\delta)S_{2i-1}.S_{2i} + J(1+\delta)S_{2i}.S_{2i+1}] \quad \text{(C1)}$$

$$H_{SP}^{63} = \sum_{i=-1}^{-15} [J(1+\delta)S_{2i-1}.S_{2i} + J(1-\delta)S_{2i}.S_{2i+1}] + J_P S_{-1}.S_{+1} + \sum_{i=1}^{15} [J(1+\delta)S_{2i-1}.S_{2i} + J(1-\delta)S_{2i}.S_{2i+1}] + J(1+\delta)S_{31}.S_{32} \quad \text{(C2)}$$

Fig. 12(a) shows the first fifty eigenvalues of H_{SP}^{62} and H_{SP}^{63} calculated for $J_P/J = 0.1$. In both cases an important gap of energy of about $\Delta/J = 0.30$ between the ground state and the quasi-continuum exists and this gap is directly related to the dimerization parameter δ by $\Delta/J = 2\delta^{3/4}$. In the case N = 62 we can see a smaller gap of $\Delta_S/J = 0.035$ between the ground state and the first excited one. Fig. 12(b) shows the effect of J_P/J on the gap Δ_S/J. The relation is linear and we extract a slope of 0.35.

We used the Quantum Monte Carlo method to calculate the susceptibility of H_{SP}^{62} as a function of temperature from 0.005 J to 0.5 J, which, taking $J = 600$ K from experimental data (see Sec. III A 1) corresponds to $T = 3$ K to 300 K . For this purpose we use the QMC algorithm "looper" which shows the best performance for Heisenberg models. The susceptibility χ shown on the figure 12(c) was calculated for $J_P = 60$ K. In the low temperature regime ($T < 50$ K) the susceptibility matches with the Bleaney-Bowers formula [78] with a gap of $\Delta_S = 21$ K. The B-B formula is the analytical form of the susceptibility for two spins 1/2 coupled by an isotropic exchange. Here we have two spins 1/2 made of tens of spins coupled by J_P and we showed by DMRG

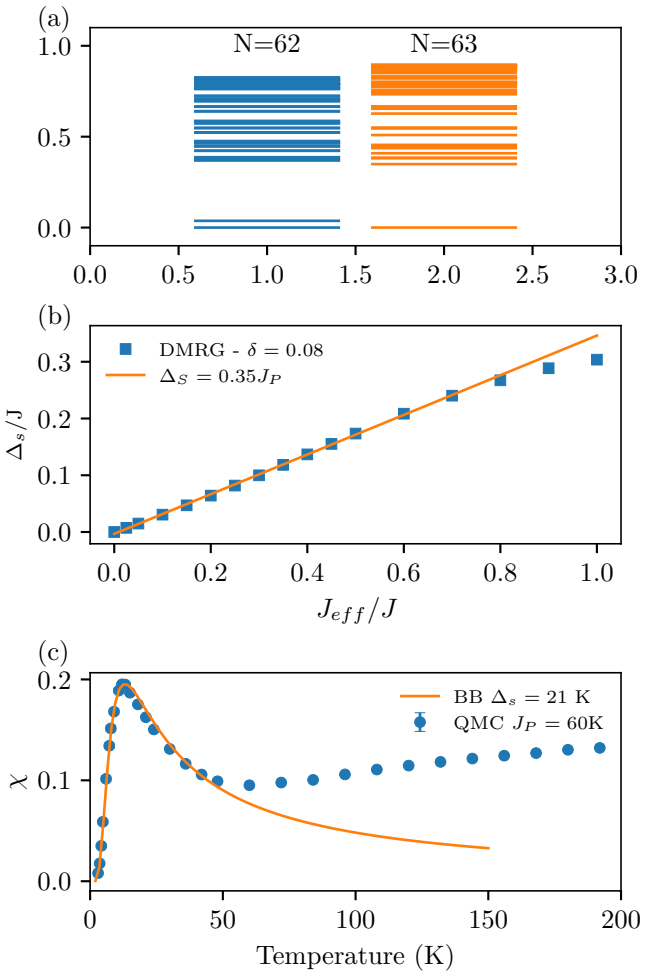

Figure 12. (a) Energy spectra of a dimerized spin chain containing a defect in the middle of the chain (according to model in Fig. 8). For even number of spins the $S_z = 0$ are shown, while for odd number of spins the $S_z = \frac{1}{2}$ are presented. Calculation are performed by DMRG. (b) Variation of the first gap Δ_S of the pair of solitons between the ground state and the first excited state as function of the effective coupling J_P. (c) Susceptibility of the pair of solitons using $J_P = 60$ K calculated by QMC. At low enough temperature the susceptibility can be described by the Bleaney and Bowers formula but with a renormalized gap (solid curve). At high temperatures the quasi-continuum is populated and the system cannot be treated as a pair of spins $\frac{1}{2}$

.

$\Delta_S = 0.35 J_P$. The B-B formula give a fair description : 21 K/60 K = 0.35 if the gap Δ_S is renormalized by 0.35.

Appendix D: Dipolar field

In order to evaluate the dipole-dipole contribution to the anisotropy parameter d, we adopted a spin distribution around the defect as shown in Fig. 13, all sites being equally spaced with a period of $a = 7$ Å. The values of

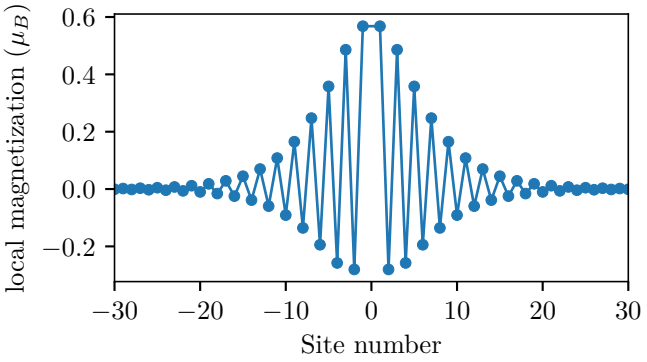

Figure 13. Local magnetization computed by DMRG of a pair of solitons in a triplet state, $S = 1$, $S_z = 1$ pinned to a defects in site 0.

the magnetic moments were taken from our previous calculation with the DMRG code of Ref. [34]:

$$\mu_1 = 0.57\,\mu_B, \quad \mu_2 = -0.28\,\mu_B, \quad \mu_3 = 0.49\,\mu_B,$$
$$\mu_4 = -0.26\,\mu_B, \quad \mu_5 = 0.36\,\mu_B, \quad \text{etc.}$$

with $\mu_{-i} = \mu_i$. The dipole-dipole sum,

$$d = \frac{4}{\mu_B a^3} \sum_{i=1}^{N} \sum_{j=1}^{N} \frac{\mu_i \mu_j}{(i+j)^3} \,, \tag{D1}$$

converges rapidly as $N \to \infty$. The final result, $d = 4.0$ G, is obtained with $N \geq 5$. But even a quick estimate with $N = 1$ produces a value that is only 10% too high, $d = \mu_1^2/2\mu_B a^3 = 4.4$ G. Both theoretical estimates agree within 5% with the value deduced from the experimental data of Fig. 7(b), $d = 4.2$ G.

[1] R. M. White, *Quantum Theory of Magnetism*, 2nd ed., Springer Series in Solid-State Sciences No. 32 (Springer Springer, Berlin New-York, 1983).
[2] A. N. Vasiliev, ed., *Low-Dimensional Magnetism* (CRC Press, Taylor & Francis Group, Boca Raton, 2019).
[3] H. Bethe, Z. Phys. **71**, 205 (1931).
[4] H. Alloul, J. Bobroff, M. Gabay, and P. J. Hirschfeld, Rev. Mod. Phys. **81**, 45 (2009).
[5] P. Foury-Leylekian, S. Petit, C. Coulon, B. Hennion, A. Moradpour, and J.-P. Pouget, Phys. B Condens. Matter **404**, 537 (2009).
[6] L. Regnault, M. Aïn, B. Hennion, G. Dhalenne, and A. Revcolevschi, Phys. Rev. B Condens. Matter **53**, 5579 (1996).
[7] D. Khomskii and M. Mostovoy, Z. Für Phys. B Condens. Matter **103**, 209 (1997).
[8] M. Nishino, H. Onishi, K. Yamaguchi, and S. Miyashita, Phys. Rev. B **62**, 9463 (2000).
[9] E. Sørensen, I. Affleck, D. Augier, and D. Poilblanc, Phys. Rev. B **58**, R14701 (1998).
[10] J. H. Shim, S. Bertaina, S. Gambarelli, T. Mitra, A. Müller, E. I. Baibekov, B. Z. Malkin, B. Tsukerblat, and B. Barbara, Phys. Rev. Lett. **109**, 050401 (2012).
[11] B. Tsukerblat, A. Tarantul, and A. Muller, Phys. Lett. A **353**, 48 (2006).
[12] L. Soriano, J. Zeisner, V. Kataev, O. Pilone, M. Fourmigue, O. Jeannin, H. Vezin, M. Orio, and S. Bertaina, Appl. Magn. Reson. **51**, 1307 (2020).
[13] S. Bertaina, C.-E. Dutoit, J. Van Tol, M. Dressel, B. Barbara, and A. Stepanov, Phys. Rev. B **90**, 060404 (2014).
[14] J. Zeisner, O. Pilone, L. Soriano, G. Gerbaud, H. Vezin, O. Jeannin, M. Fourmigué, B. Büchner, V. Kataev, and S. Bertaina, Phys. Rev. B **100**, 224414 (2019).
[15] S. Bose, Phys. Rev. Lett. **91**, 207901 (2003).
[16] L. Campos Venuti, C. Degli Esposti Boschi, and M. Roncaglia, Phys. Rev. Lett. **96**, 247206 (2006).
[17] M. Dressel, Naturwissenschaften **94**, 527 (2007).
[18] C. Coulon and R. Clérac, Chem. Rev. **104**, 5655 (2004).
[19] J. P. Pouget, Phys. B Condens. Matter **407**, 1762 (2012).
[20] M. de Souza and J.-P. Pouget, J. Phys. Condens. Matter **25**, 343201 (2013).
[21] J.-P. Pouget, Comptes Rendus Physique Physique de La Matière Condensée Au XXIe Siècle: L'héritage de Jacques Friedel, **17**, 332 (2016).
[22] J.-P. Pouget, P. Alemany, and E. Canadell, Mater. Horiz. **5**, 590 (2018).
[23] S. Bertaina, J. H. Shim, S. Gambarelli, B. Z. Malkin, and B. Barbara, Phys. Rev. Lett. **113**, 109902 (2014).
[24] C.-E. Dutoit, A. Stepanov, J. van Tol, M. Orio, and S. Bertaina, J. Phys. Chem. Lett. **9**, 5598 (2018).
[25] A. Abderraba, R. Laversanne, E. Dupart, C. Coulon, P. Delhaes, and C. Hauw, J. Phys. Colloques **44**, C3 (1983).
[26] M. Fourmigué, E. W. Reinheimer, K. R. Dunbar, P. Auban-Senzier, C. Pasquier, and C. Coulon, Dalton Trans. **2008**, 4652 (2008).
[27] P. Foury-Leylekian, P. Auban-Senzier, C. Coulon, O. Jeannin, M. Fourmigué, C. Pasquier, and J.-P. Pouget, Phys. Rev. B **84**, 195134 (2011).
[28] P. Auban-Senzier, C. R. Pasquier, O. Jeannin, and M. Fourmigué, Physica B: Condensed Matter Proceedings of the International Workshop on Electronic Crystals (ECRYS-2011), **407**, 1700 (2012).
[29] E. W. Reinheimer, A. Assaf, O. Jeannin, A. Benallouche, P.-T. Nguyen, C. Coulon, and M. Fourmigué, Phys. Status Solidi B **249**, 943 (2012).
[30] P. Hansen, D. Augier, J. Riera, and D. Poilblanc, Phys. Rev. B **59**, 13557 (1999).
[31] S. Eggert and I. Affleck, Phys. Rev. B **46**, 10866 (1992).
[32] M. Nishino, H. Onishi, P. Roos, K. Yamaguchi, and S. Miyashita, Phys. Rev. B **61**, 4033 (2000).
[33] D. Augier, E. Sørensen, J. Riera, and D. Poilblanc, Phys. Rev. B **60**, 1075 (1999).
[34] B. Bauer, L. D. Carr, H. G. Evertz, A. Feiguin, J. Freire, S. Fuchs, L. Gamper, J. Gukelberger, E. Gull, S. Guertler, A. Hehn, R. Igarashi, S. V. Isakov, D. Koop, P. N. Ma, P. Mates, H. Matsuo, O. Parcollet, G. Paw\lowski, J. D. Picon, L. Pollet, E. Santos, V. W. Scarola, U. Schollwöck, C. Silva, B. Surer, S. Todo, S. Trebst, M. Troyer, M. L. Wall, P. Werner, and S. Wessel, J. Stat. Mech. Theory Exp. **2011**, P05001 (2011).

[35] G. Wolfowicz, F. J. Heremans, C. P. Anderson, S. Kanai, H. Seo, A. Gali, G. Galli, and D. D. Awschalom, Nat Rev Mater **6**, 906 (2021).

[36] C. Coulon, G. Lalet, J. Pouget, P. Foury-Leylekian, A. Moradpour, and J. Fabre, Phys. Rev. B **76**, 1 (2007).

[37] See Supplemental Material online for ESR spectra examples, complementary susceptibility data, Rabi field sweep for the 3 compounds, residue analysis of X=Cl and X=I and python code used for the Johnston *et al.* model.

[38] D. C. Johnston, R. K. Kremer, M. Troyer, X. Wang, A. Klümper, S. L. Bud'ko, A. F. Panchula, and P. C. Canfield, Phys. Rev. B **61**, 9558 (2000), arXiv:cond-mat/0003271.

[39] L. Bulaevskii, Sov. Phys. - Solid State **11**, 921 (1969).

[40] J. Bonner and M. Fisher, Phys. Rev. **135**, A640 (1964).

[41] S. Eggert, I. Affleck, and M. Takahashi, Phys. Rev. Lett. **73**, 332 (1994).

[42] A. Klümper and D. C. Johnston, Phys. Rev. Lett. **84**, 4701 (2000).

[43] B. Salameh, S. Yasin, M. Dumm, G. Untereiner, L. Montgomery, and M. Dressel, Phys. Rev. B **83**, 205126 (2011).

[44] J. P. Pouget, P. Foury-Leylekian, S. Petit, B. Hennion, C. Coulon, and C. Bourbonnais, Phys. Rev. B **96**, 035127 (2017).

[45] M. Dumm, B. Salameh, M. Abaker, L. K. Montgomery, and M. Dressel, J. Phys. IV Proc. **114**, 57 (2004).

[46] P. Wzietek, F. Creuzet, C. Bourbonnais, D. Jérome, K. Bechgaard, and P. Batail, J. Phys. I France **3**, 171 (1993).

[47] A. W. Sandvik, R. R. P. Singh, and D. K. Campbell, Phys. Rev. B **56**, 14510 (1997).

[48] R. W. Kühne and U. Löw, Phys. Rev. B **60**, 12125 (1999).

[49] T. Granier, B. Gallois, L. Ducasse, A. Fritsch, and A. Filhol, Synth. Met. **24**, 343 (1988).

[50] K. Furukawa, T. Hara, and T. Nakamura, J. Phys. Soc. Jpn. **78**, 104713 (2009).

[51] M. de Souza, P. Foury-Leylekian, A. Moradpour, J.-P. Pouget, and M. Lang, Phys. Rev. Lett. **101**, 216403 (2008).

[52] D. C. Johnston, T. Saito, M. Azuma, M. Takano, T. Yamauchi, and Y. Ueda, Phys. Rev. B **64**, 134403 (2001).

[53] T. Barnes, J. Riera, and D. A. Tennant, Phys. Rev. B **59**, 11384 (1999).

[54] D. Augier, D. Poilblanc, S. Haas, A. Delia, and E. Dagotto, Phys. Rev. B **56**, R5732 (1997).

[55] E. Orignac and R. Chitra, Phys. Rev. B **70**, 1 (2004).

[56] M. Hase, I. Terasaki, and K. Uchinokura, Phys. Rev. Lett. **70**, 3651 (1993).

[57] M. Dumm, A. Loidl, B. Fravel, K. Starkey, L. Montgomery, and M. Dressel, *Electron Spin Resonance Studies on the Organic Linear-Chain Compounds (TMTCF)2X (C=S,Se; X=PF6,AsF6,ClO4,Br)*, Vol. 61 (APS, 2000).

[58] J. L. Black and V. J. Emery, Phys. Rev. B **23**, 429 (1981).

[59] M. C. Cross and D. S. Fisher, Phys. Rev. B **19**, 402 (1979).

[60] G. Spronken, B. Fourcade, and Y. Lépine, Phys. Rev. B **33**, 1886 (1986).

[61] T. Papenbrock, T. Barnes, D. J. Dean, M. V. Stoitsov, and M. R. Strayer, Phys. Rev. B **68**, 024416 (2003).

[62] E. Orignac, Eur. Phys. J. B **39**, 335 (2004).

[63] C. Rovira, J. Tarrés, J. Llorca, E. Molins, J. Veciana, S. Yang, D. O. Cowan, C. Garrigou-Lagrange, J. Amiell, P. Delhaes, E. Canadell, and J. P. Pouget, Phys. Rev. B **52**, 8747 (1995).

[64] P. Fertey, M. Poirier, M. Castonguay, J. Jegoudez, and A. Revcolevschi, Phys. Rev. B **57**, 13698 (1998).

[65] D. Smirnov, P. Millet, J. Leotin, D. Poilblanc, J. Riera, D. Augier, and P. Hansen, Phys. Rev. B **57**, R11035 (1998).

[66] S. Fujimoto and S. Eggert, Phys. Rev. Lett. **92**, 037206 (2004).

[67] S. Fujimoto and S. Eggert, J. Phys. Soc. Jpn. **74**, 36 (2005).

[68] T. Ami, M. Crawford, R. Harlow, Z. Wang, D. Johnston, Q. Huang, and R. Erwin, Phys. Rev. B **51**, 5994 (1995).

[69] Y. Utz, F. Hammerath, R. Kraus, T. Ritschel, J. Geck, L. Hozoi, J. van den Brink, A. Mohan, C. Hess, K. Karmakar, S. Singh, D. Bounoua, R. Saint-Martin, L. Pinsard-Gaudart, A. Revcolevschi, B. Büchner, and H.-J. Grafe, Phys. Rev. B **96**, 115135 (2017).

[70] A. I. Smirnov, V. N. Glazkov, L. I. Leonyuk, A. G. Vetkin, and R. M. Eremina, J. Exp. Theor. Phys. **87**, 1019 (1998).

[71] C. Coulon, P. Foury-Leylekian, J.-M. Fabre, and J.-P. Pouget, Eur. Phys. J. B **88**, 85 (2015).

[72] J. Zeisner, O. Pilone, L. Soriano, G. Gerbaud, H. Vezin, O. Jeannin, M. Fourmigué, B. Büchner, V. Kataev, and S. Bertaina, ArXiv190910301 Cond-Mat (2019), arXiv:1909.10301 [cond-mat].

[73] I. S. Camara, R. Gautier, E. Le Fur, J.-C. Trombe, J. Galy, A. M. Ghorayeb, and A. Stepanov, Phys. Rev. B **81**, 184433 (2010).

[74] R. E. Behringer, J. Chem. Phys. **29**, 537 (1958).

[75] L. N. Majer, B. Miksch, O. Iakutkina, T. Kobayashi, A. Kawamoto, and M. Dressel, Phys. Rev. B **102**, 214430 (2020).

[76] M. Orio, J. K. Bindra, J. van Tol, M. Giorgi, N. S. Dalal, and S. Bertaina, J. Chem. Phys. **154**, 154201 (2021).

[77] A. Schweiger and G. Jeschke, *Principles of Pulse Electron Paramagnetic Resonance*, reprinted ed. (Oxford Univ. Press, Oxford, 2005).

[78] B. Bleaney and K. D. Bowers, Proc. R. Soc. Lond. Ser. Math. Phys. Sci. **214**, 451 (1952).

[79] S. Sahling, G. Remenyi, C. Paulsen, P. Monceau, V. Saligrama, C. Marin, A. Revcolevschi, L. P. Regnault, S. Raymond, and J. E. Lorenzo, Nat. Phys. **11**, 255 (2015).

[80] F. Neese, Wiley Interdiscip. Rev. Comput. Mol. Sci. **2**, 73 (2012).

[81] A. D. Becke, J. Chem. Phys. **98**, 1372 (1993).

[82] C. Lee, W. Yang, and R. G. Parr, Phys. Rev. B **37**, 785 (1988).

[83] A. Schäfer, C. Huber, and R. Ahlrichs, J. Chem. Phys. **100**, 5829 (1994).

[84] F. Weigend, Phys. Chem. Chem. Phys. **8**, 1057 (2006).

[85] A. Klamt and G. Schüürmann, J Chem Soc Perkin Trans 2 , 799 (1993).

[86] S. Grimme, J. Antony, S. Ehrlich, and H. Krieg, J. Chem. Phys. **132**, 154104 (2010).

[87] L. Noodleman and E. R. Davidson, Chemical Physics **109**, 131 (1986).

[88] L. Noodleman and D. A. Case, in *Advances in Inorganic Chemistry*, Vol. 38, edited by R. Cammack (Academic Press, 1992) pp. 423–470.

[89] L. Noodleman, J. Chem. Phys. **74**, 5737 (1981).

[90] T. Soda, Y. Kitagawa, T. Onishi, Y. Takano, Y. Shigeta, H. Nagao, Y. Yoshioka, and K. Yamaguchi, Chemical Physics Letters **319**, 223 (2000).

Supplementary Information

Electron spins interaction in the spin-Peierls phase of the organic spin chain $(o\text{-DMTTF})_2X$ (X = Cl, Br, I)

ESR SPECTRA

The data presented in the manuscript have been obtained by least-square fitting using this equation:

$$I_{ESR} = A\left(\frac{\Gamma\cos\phi}{\Gamma^2+(H-H_0)^2}+\frac{(H-H_0)\sin\phi}{\Gamma^2+(H-H_0)^2}\right) \tag{S1}$$

where A is directly proportional to the spin susceptibility. H_0 is the resonance field which using the relation $g\mu_B H_0 = h\nu$ give us the g factor. Γ is the half width at half maximum and ϕ the dispersion angle. Γ and ϕ where mostly identical than the ones reported with a high accuracy in Ref. [27].

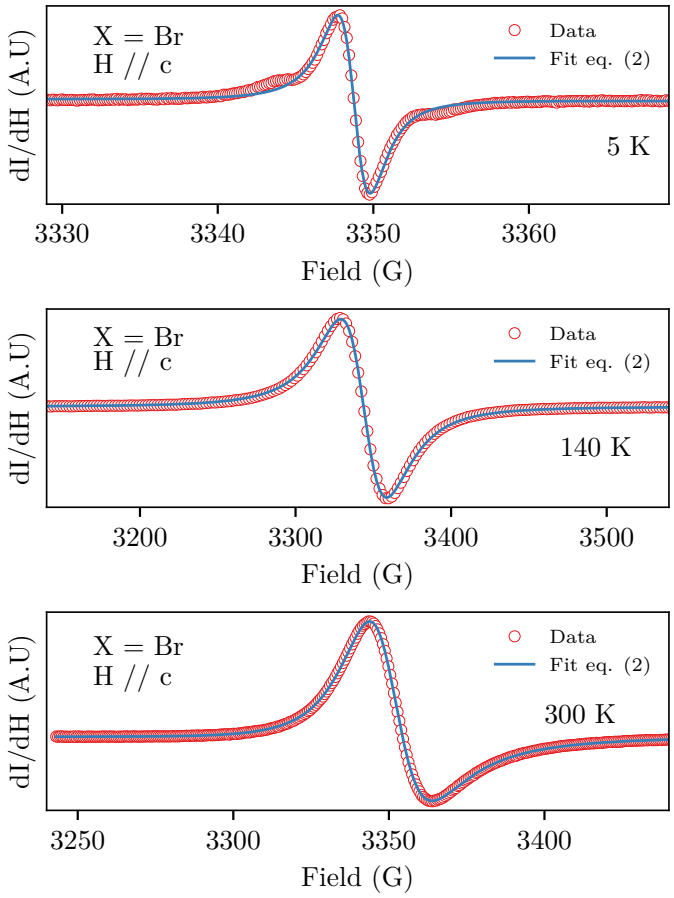

Figure S1. Examples of ESR spectra recorded for $(o\text{-DMTTF})_2$Br at 5K, 140K and 300K. The blue line is the best fit using eq. (2) of the main text or (S1).

Fig. S1 present some examples of data and fit curves. Note the large variation of magnetic field scale with the temperature.

It is also important noticing the difficulty to observe the satellite lines which tend to saturate easily and so can become unresolved if the microwave power is to large (see Fig S2).

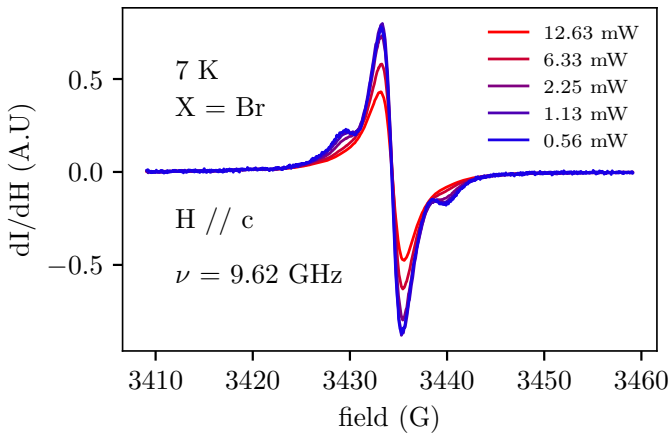

Figure S2. Microwave power dependence of ESR signal is (o-DMTTF)$_2$Br at 7K.

ANALYSIS OF SUSCEPTIBILITY

Figure S3 presents the corrected susceptibility of (o-DMTTF)$_2$Cl as a function of temperature. The spin chain is uniform above $T_{SP} = 50$ K. In this temperature range we used the method described in the section III.A.1 of main text to evaluate $J_{eff}(T)$ presented in the inset of figure S3 . For $T < T_{SP}$ the Spin-Peierls transition occurs and the gapless uniform spin chains become progressively dimerized and gapped spin chains. The EPR susceptibility is in a good agreement with DC susceptibility from previous SQUID measurements [27].

The data from figure S4 are adapted from the Bulaevskii [39] calculations on dimerized spin chains. In the Hartree-Fock approximation and from the hamiltonian (S2) he evaluated the temperature dependences of the susceptibilities for different values of γ. At low temperature the analytic form $x(T, \gamma)$ is a good approximation with the values $\alpha(\gamma)$ and $\Delta(\gamma)$ presented in figure S4.

$$H = \sum_n S_{2n-1}.S_{2n} + \gamma S_{2n}.S_{2n+1} \tag{S2}$$

$$x(T, \gamma) = \frac{\alpha(\gamma)}{T} e^{J_{max}\Delta(\gamma)/T} \tag{S3}$$

Figure S6 regroups the same data and fit parameters as in the figure 10 of the main text. On the figure S6.b we obtain χ_{tot}-χ_{Curie} by substracting the Curie law part of eq.(6) to χ_{tot}. For (o-DMTTF)$_2$Cl and (o-DMTTF)$_2$Br χ_{tot}-χ_{Curie} follow the characteristic form of Bowers-Bleaney [78] model respectively with Δ_s(Cl) = 16.7 K and Δ_s(Br) = 20.3 K. The susceptibility χ_{tot}-χ_{Curie} of (o-DMTTF)$_2$I is approximatively equal to zero in the temperature range [5 K, 25 K] and for this reason we think no S=1 gapped system exist in it.

An example of determination of the dimerization parameter δ by different methods using χ_{ESR} for (o-DMTTF)$_2$Br is given in fig.S5. The model labeled "Bulaevski free amplitude (Bul. FA)" corresponds to eq. (3) with α and ΔB regarded as independent while "Bulaevski" is eq. (3) with only δ as a free parameter. "Johnston et al. " is a direct numerical calculation of the susceptibility using TMRG with only δ as a free parameter. At first sight Bul. FA seems a better fit, but a closer look at low temperature on the log-log scale (Fig.S5 inset) detects an important discrepancy with the data. On the contrary, the two other models used, correctly show a very good agreement with experimental data for T < 40 K. At higher temperature the dimerization δ(T) decreases and the models cannot be used in the current form any more. Let us note a large overestimation of δ in the Bul. FA it while Bulaevski and Johnston et al. fits produce rather consistent values of δ, those of Bulaevski being slightly higher.

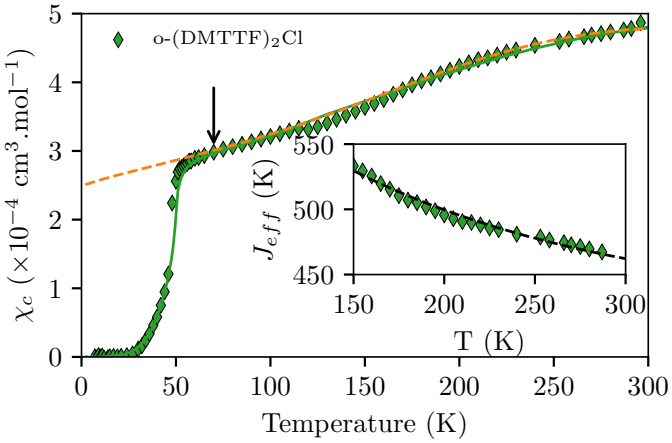

Figure S3. Temperature dependence of the spin susceptibility corrected by the Curie tail of $S = 1/2$ defects χ_c of (o-DMTTF)$_2$Cl. The dashed lines are the theoretical values of the susceptibility using exchange constants J_{eff} . The plain line is the susceptibility obtained by SQUID [27]

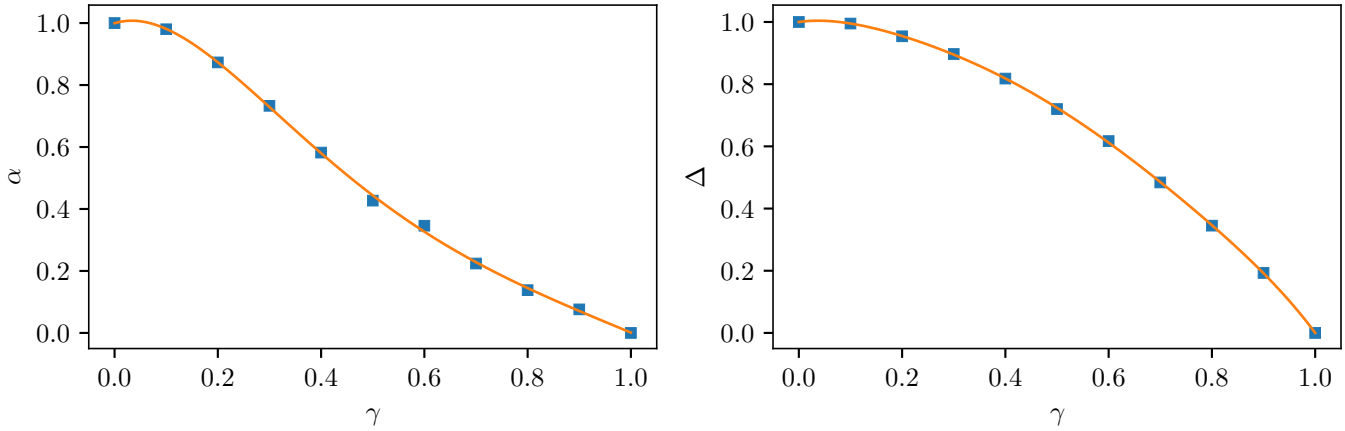

Figure S4. Bulaevski calculation [39] of a dimerized chain. The intensity α and gap Δ as function of γ=$\frac{1-\delta}{1+\delta}$ calculated by Bulaevskii are presented by squares. The plain lines are polynomial fit used to interpolate data to any values of γ .

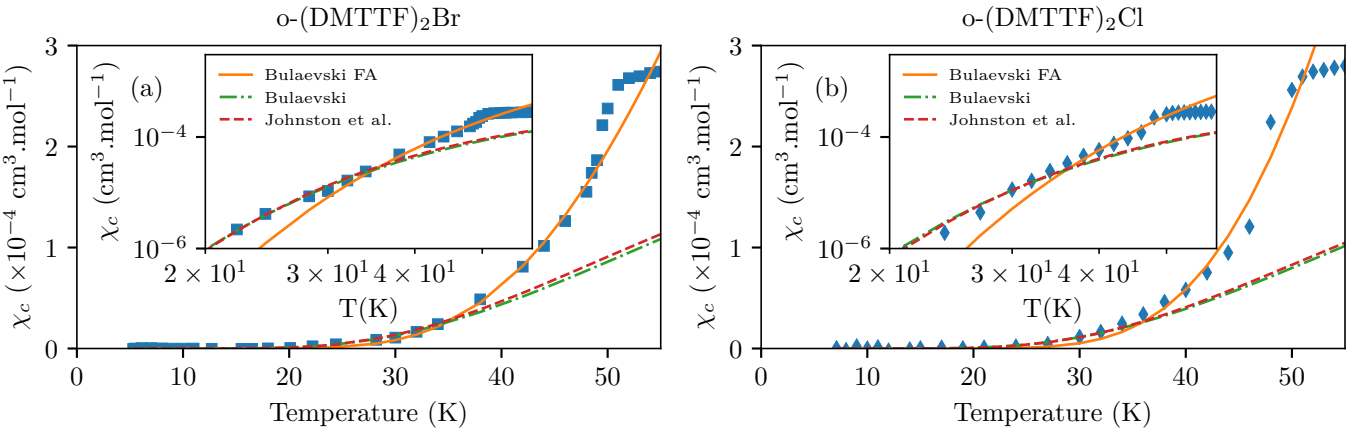

Figure S5. (a) Temperature dependence of the spin susceptibility in the low-temperature region for (o-DMTTF)$_2$Br. (b) Temperature dependence of the spin susceptibility in the low-temperature region for (o-DMTTF)$_2$Cl. Below $T_{SP} = 50$ K the susceptibility drops to the non-magnetic spin-Peierls state. The plain orange lines are the best fits using eq.(3) taking α and Δ as two independent fit parameters. The green dashed dots and red dashed lines are the best fits for the Bulaevskii and Johnston et al. model respectively using only δ as a fit parameter. The insets are the log-log scale of the figures, magnifying the discrepancy of the Bulaevskii FA model at low temperature.

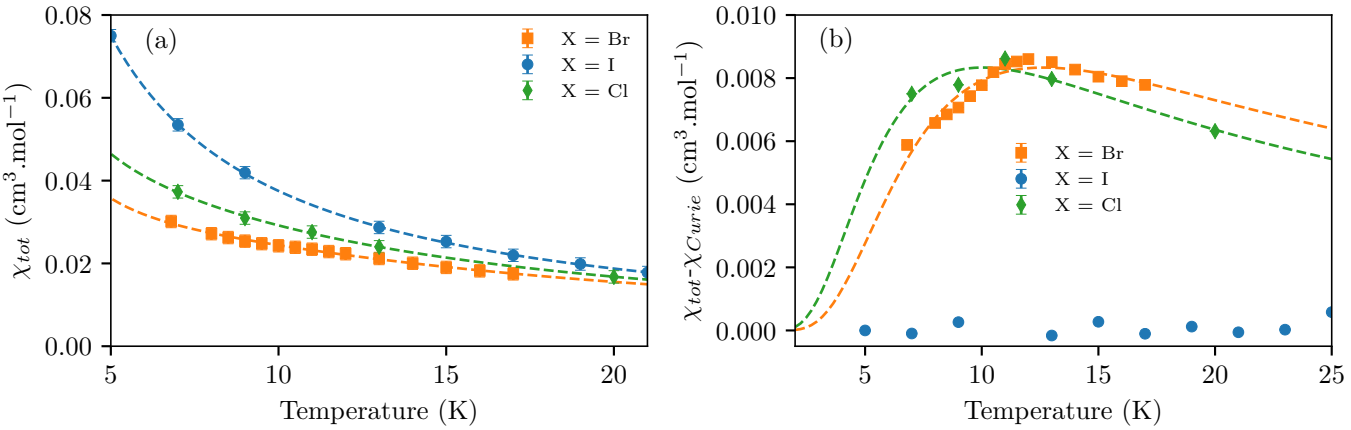

Figure S6. (a) Temperature dependence of the spin susceptibility in the low-temperature region for (o-DMTTF)$_2$Br, X = Cl, Br and I. The dashed lines are the best fit using eq.(6). (b) Difference between the susceptibility χ_{tot} and the Curie law component in eq.(6). The dashed lines are the best fit of χ_{tot} using eq.(6) without the Curie law component.

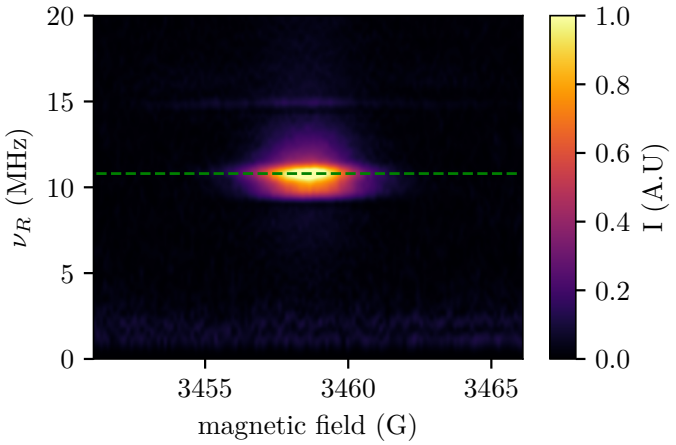

Figure S7. Image plot of the FFT of the Rabi oscillations of (o-DMTTF)$_2$I for H_0 // c, T = 5.8 K and h_{mw} = 4 G.We used the three-pulse sequence described in experimental details.

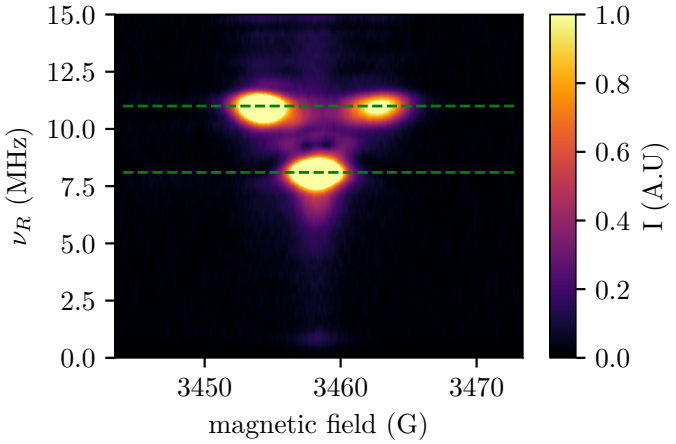

Figure S8. Image plot of the FFT of the Rabi oscillations of (o-DMTTF)$_2$Br for H_0 // c, T = 5.4 K and h_{mw} = 2.7 G.We used the three-pulse sequence described in experimental details.

RABI FIELD SWEEP

The figure S7,S8 and S9 show the FFT of the Rabi oscillations on (o-DMTTF)$_2X$ (X = Cl, Br and I) sweeping the magnetic field. We can clearly identify two different Rabi frequencies at $\nu_R^{S=1/2}$ = 7.6 MHz and $\nu_R^{S=1}$ = 11 MHz in (o-DMTTF)$_2$Br. The two spots attributed to S = 1 are separated by $\sim$ 8 G. On (o-DMTTF)$_2$Cl the S= 1/2 system oscillates at $\nu_R^{S=1/2}$ = 6.1 MHz and one can see a faint large spot at $\nu_R^{S=1}$ = 8.5 MHz . The figure S7 confirms that only S = 1/2 exist in (o-DMTTF)$_2$I only a spot at $\nu_R^{S=1/2}$ = 11 MHz is visible.

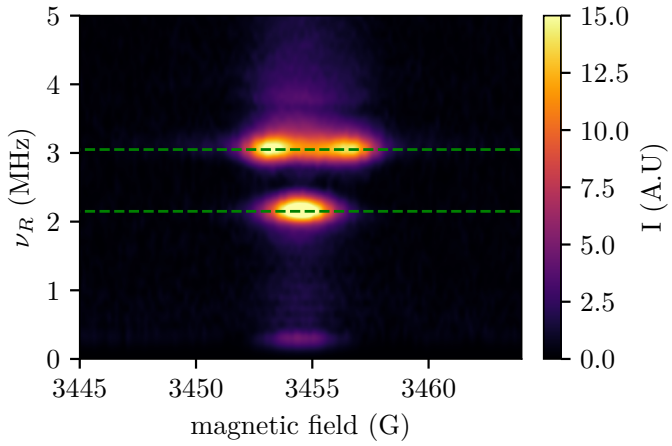

Figure S9. Image plot of the FFT of the Rabi oscillations of (o-DMTTF)$_2$Cl for H_0 //, T = 5.5 K and h_{mw} = 0.75 G .We used the three-pulse sequence described in experimental details.

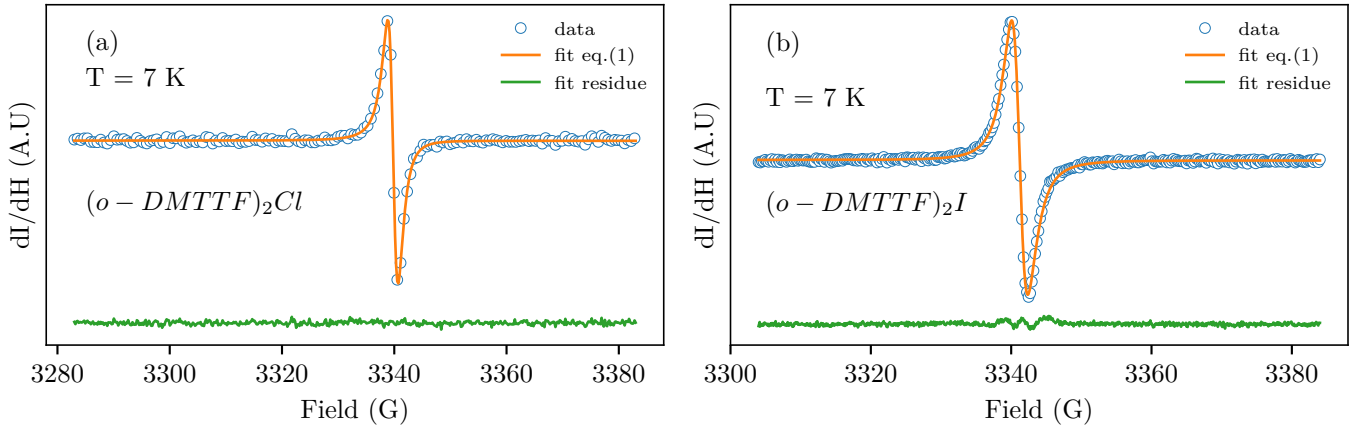

Figure S10. (a) Example of ESR signal of for(o-DMTTF)$_2$Cl and (b) (o-DMTTF)$_2$I at T = 7 K and magnetic field H // c. The central lines have been fitted using a derivative of a lorentzian (orange lines). The residues of the fits are represented by the green line.

EPR SPECTRA, FIT AND RESIDUE

On the figure S10 the spectra of (o-DMTTF)$_2$Cl and (o-DMTTF)$_2$I are fitted with a dispersive lorentzian model are presented. This fit is really suitable for (o-DMTTF)$_2$Cl for every orientations and gives a very small residue. The (o-DMTTF)$_2$I residue is bigger because the line is not exactly lorentzian.By looking at the angular dependence ... on the figure 7 of the main text.

PROBABILITY OF PAIRED AND SINGLE SOLITONS

In the main text we have provide an explanation of 50/50% change for having a paired or a single soliton. Here we list all the possible configurations with: odd number of spins with the soliton on the right O_R of on the left O_L and the even number of spins with strong links on the edge E_S or weak links E_W. Only the result around the defect is considered. 8 configurations give a single soliton and 4 give paired solitons leading to 50/50%

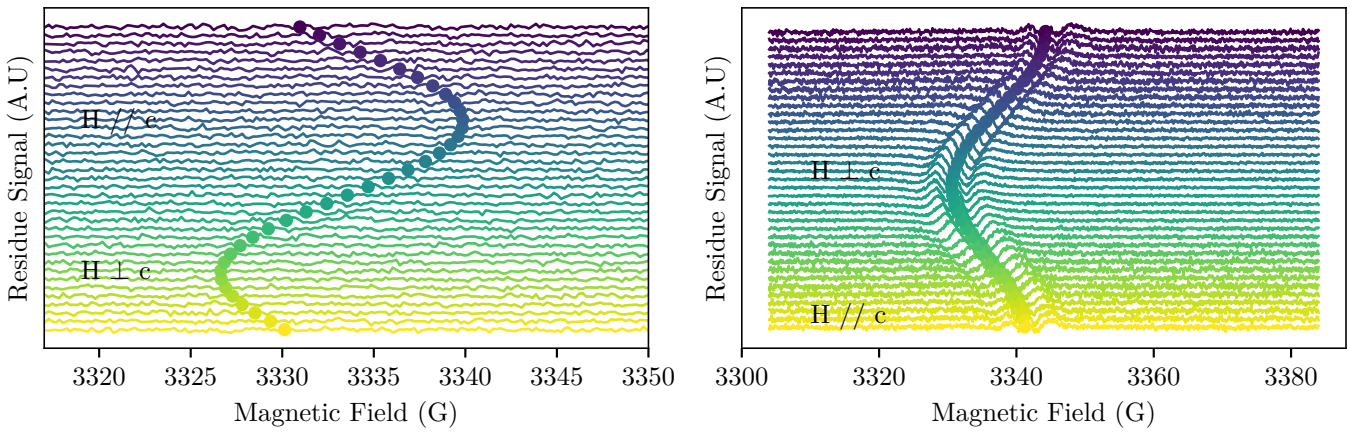

Figure S11. Angular dependence of the fit residue of (o-DMTTF)$_2$Cl (left) and (o-DMTTF)$_2$I (right) at 7 K. The circles show the resonance field of the central line.

Table S1. List of the configurations. The defect is between the "left chain" and the "right chain". Around the defect, the spin chain ca be odd number of spins with the non dimerized spin on the left O_L or the right O_R, or even number of spins with strong link E_S or weak link E_W on the edge.

Left chain	Right chain	Nature
E_W	E_W	Paired
E_W	E_S	Single
E_W	O_L	Paired
E_W	O_R	Single
E_S	E_W	Single
E_S	E_S	None
E_S	O_L	Single
E_S	O_R	None
O_L	E_W	Single
O_L	E_S	None
O_L	O_L	Single
O_L	O_R	None
O_R	E_W	Paired
O_R	E_S	Single
O_R	O_L	Paired
O_R	O_R	Single

PYTHON CODE FOR JOHNSTON *ET AL.* SUSCEPTIBILITY

```
#!/usr/bin/python
# -*- coding: utf-8 -*-

import numpy as np

def chi_J(t, a):
""" Chi_star as a function of temperature according to
Johnston et al. (2000) p. 9578 for S = 1/2 HAF chain
t ... reduced temperature (k_B*T/Jmax)
a ... asymmetry parameter alpha = (J2/J1) =(1-delta)/(1+delta)
values for Nmn and Dmn parameters are taken from Table II in Johnston et al.
(2000) """

delta_fit = 1. - 0.5 * a - 2. * a ** 2 + 1.5 * a ** 3
g1 = 0.38658545
g2 = -0.20727806
delta_0 = (1. - a) ** 0.75 * (1. + a) ** 0.25 + g1 * a * (1. - a) \
+ g2 * a ** 2 * (1. - a) ** 2
N0 = 1.
N1 = 0.63427990 - 2.06777217 * a - 0.70972219 * a ** 2 + 4.89720885 \
* a ** 3 - 2.80783223 * a ** 4
N2 = 0.18776962 - 2.84847225 * a + 5.96899688 * a ** 2 - 3.85145137 \
* a ** 3 + 0.64055849 * a ** 4
N3 = 0.033603617 - 0.757981757 * a + 4.137970390 * a ** 2 \
- 6.100241386 * a ** 3 + 2.701116573 * a ** 4
N4 = 0.0038611069 + 0.5750352896 * a - 2.3359243110 * a ** 2 \
+ 2.934083364 * a ** 3 - 1.1756629304 * a ** 4
N5 = 0.00027331430 - 0.10724895512 * a + 0.40345647304 * a ** 2 \
- 0.48608843641 * a ** 3 + 0.18972153852 * a ** 4
N6 = 0.00578123759 * a - 0.02313572892 * a ** 2 + 0.02892774508 * a \
** 3 - 0.01157325374 * a ** 4
N71 = 2.59870347E-7
N72 = -2.39236193E-7
sum_Nn = N0 + N1 / t + N2 / t ** 2 + N3 / t ** 3 + N4 / t ** 4 + N5 \
/ t ** 5 + N6 / t ** 6
D0 = 1.
D1 = -0.11572010 - 1.31777217 * a + 1.29027781 * a ** 2 \
+ 3.39720885 * a ** 3 - 2.80783223 * a ** 4
D2 = 0.08705969 - 1.44693321 * a + 5.09401919 * a ** 2 \
- 10.51861382 * a ** 3 + 8.97655318 * a ** 4 + 5.75312680 * a \
** 5 - 11.83647774 * a ** 6 + 4.21174835 * a ** 7
D3 = 0.00563137 + 0.65986015 * a - 1.38069533 * a ** 2 - 0.09849603 \
* a ** 3 + 7.54214913 * a ** 4 - 22.31810507 * a ** 5 \
+ 27.60773633 * a ** 6 - 6.39966673 * a ** 7 - 15.69691721 * a \
** 8 + 13.37035665 * a ** 9 - 3.15881126 * a ** 10
D4 = 0.0010408866 + 0.1008789796 * a - 0.9188446197 * a ** 2 \
+ 1.6052570070 * a ** 3 - 0.7511481272 * a ** 4
D5 = 0.0000683286 - 0.1410232710 * a + 0.6939435034 * a ** 2 \
- 0.9608700949 * a ** 3 + 0.4106951428 * a ** 4
D6 = 0.0367159872 * a - 0.1540749976 * a ** 2 + 0.1982667100 * a \
** 3 - 0.0806430233 * a ** 4
D7 = -0.00314381636 * a + 0.01140642324 * a ** 2 - 0.01338139741 \
* a ** 3 + 0.00511879053 * a ** 4
D81 = 1.25124679E-7
D82 = -1.03824523E-7
sum_Dn = D0 + D1 * t ** -1 + D2 * t ** -2 + D3 * t ** -3 + D4 * t \
** -4 + D5 * t ** -5 + D6 * t ** -6 + D7 * t ** -7
y = 4.69918784
z = 3.55692695
Pade_approx = (sum_Nn + (N71 * a + N72 * a ** 2) * (delta_0 / t)
** y * t ** -7) / (sum_Dn + (D81 * a + D82 * a ** 2)
* (delta_0 / t) ** z * np.exp((delta_0 - delta_fit) / t)
* t ** -8)
chi_star = Pade_approx * np.exp(-delta_fit / t) / (4 * t)
return 0.3751 * 2.01 ** 2 / J * chi_star
```